

Multistatic Imaging of Extended Targets*

Habib Ammari[†], Josselin Garnier[‡], Hyeonbae Kang[§], Mikyoung Lim[¶], and Knut Sølna^{||}

Abstract. In this paper we develop iterative approaches for imaging extended inclusions from multistatic response measurements at single or multiple frequencies. Assuming measurement noise, we perform a detailed stability and resolution analysis of the proposed algorithms in two different asymptotic regimes. We consider both the Born approximation in the nonmagnetic case and a high-frequency regime in the general case. Based on a high-frequency asymptotic analysis of the measurements, an algorithm for finding a good initial guess for the illuminated part of the inclusion is provided and its optimality is shown. The initial guess, obtained through standard statistical arguments, turns out to be Kirchhoff migration. We illustrate the efficiency and the limitations of the proposed algorithms with a variety of numerical examples.

Key words. extended target, shape recovery, multistatic imaging, weighted subspace migration, stability and resolution analysis, optimal control

AMS subject classifications. 35R30, 35B30

DOI. 10.1137/10080631X

1. Introduction. Recently, we have been interested in the problem of locating and estimating the geometric features of small inclusions (compared to the operating wavelength), using arrays of point source transmitters and receivers at single or multiple frequencies. This measurement configuration gives the so-called multistatic response matrix (MSR). In [9], using long-wavelength asymptotic expansions of the measurements, we have shown how the electromagnetic parameters and the equivalent ellipse of the target can be reconstructed. We have also proposed an optimization approach to image geometric details of the target that are finer than the equivalent ellipse.

In this paper, we consider extended inclusions, i.e., of characteristic size much larger than half the operating wavelength. Our purpose is to propose iterative approaches for imaging them from MSR measurements at single or multiple frequencies. Since the structure of MSR matrices in this case is quite complicated, a direct approach cannot be developed for imaging extended inclusions. However, direct approaches can be used to construct a good initial guess.

*Received by the editors August 23, 2010; accepted for publication (in revised form) December 19, 2011; published electronically April 12, 2012. This work was supported by the National Institute for Mathematical Sciences (2010 Thematic Program, TP1003), the Korea Research Foundation through grant KRF-2008-220-C00002, NRF grants 2009-0090250 and 2010-0017532, and NSF grant DMS0709389.

<http://www.siam.org/journals/siims/5-2/80631.html>

[†]Department of Mathematics and Applications, Ecole Normale Supérieure, 45 Rue d'Ulm, 75005 Paris, France (habib.ammari@ens.fr).

[‡]Laboratoire de Probabilités et Modèles Aléatoires and Laboratoire Jacques-Louis Lions, Université Paris VII, 2 Place Jussieu, 75251 Paris Cedex 5, France (garnier@math.jussieu.fr).

[§]Department of Mathematics, Inha University, Incheon 402-751, Korea (hbkang@inha.ac.kr).

[¶]Department of Mathematical Sciences, Korean Advanced Institute of Science and Technology, Daejeon 305-701, Korea ([mklim@kaist.ac.kr](mailto:mklin@kaist.ac.kr)).

^{||}Department of Mathematics, University of California, Irvine, CA 92697 (ksolna@math.uci.edu).

We first provide new optimization algorithms to reconstruct the inclusion shape and compare them with a standard approach which consists of minimizing the discrepancy between the computed and measured MSR matrices. Our main motivation is to provide better imaging algorithms in the sense of resolution and stability than the standard approach. Moreover, in the presence of measurement noises, a stability and resolution analysis for the proposed imaging algorithms is provided in two different asymptotic regimes. It seems extremely difficult to carry out such analytic calculations in general. To give insights into the imaging problem from MSR measurements, we consider both the Born approximation in the case where there is only a permittivity contrast and a high-frequency regime in the general case where there are both permittivity and permeability contrasts. We show that while in the Born approximation points inside the target contribute to the MSR measurements, only the ones on the illuminated part of the boundary do so in the case of both permittivity and permeability contrasts. Furthermore, we propose a weighted subspace migration imaging functional for finding a good initial guess. In the presence of white noise, we show that the weights are uniform if the illumination is uniform in the angle space and prove its optimality by using standard statistical tools. The optimality of the imaging functional for finding the initial guess is to be understood in the sense that the location of its maximum is exactly the maximum likelihood estimator of a sampling of the inclusion shape. Finally, to handle topology changes such as breaking one component into two, we develop a level-set version of our algorithms.

Our results in this paper extend those in [32, 22] on the design of direct imaging procedures within the Born approximation. The use of weights in subspace migration algorithms to emphasize information contained in the weak eigenvalues of the MSR matrix was first proposed in [17]. Here we apply the same idea to design optimal control algorithms capable of providing images with good resolution. On the other hand, level-set formulations were introduced in imaging in [29]. See also the review in [18].

The paper is organized as follows. In section 2 we formulate the imaging problem in a simplified electromagnetic setting. We consider solutions in the presence of the inclusion to the Helmholtz equation in two and three dimensions. In section 3 we introduce three different optimization algorithms to reconstruct the inclusion shape from MSR measurements. In order to minimize these three cost functionals, their shape derivatives are computed in section 4. Section 5 is devoted to the analysis of the Born approximation in the nonmagnetic (i.e., purely dielectric) case. Assuming measurement noises, we perform a resolution and stability analysis of the proposed algorithms. In section 6 we turn to the case of both permittivity and permeability contrasts and carry out a high-frequency asymptotic analysis of the MSR matrix. We show that the MSR matrix in this regime depends only on the part of the boundary of the target that is illuminated. Furthermore, we give evidence that in order to sharply detect the edges of the boundary one should choose a weight function in the cost functional that enhances the contributions of the singular vectors in the plunge region of the singular values. In section 7 we develop a weighted subspace migration imaging functional for constructing a good initial guess and show its optimality using standard statistical tools. We illustrate our main findings on the efficiency and viability of the proposed algorithms with some numerical examples in section 8. In section 9 our main results for the Helmholtz equation are extended to the elastic case. We develop three optimal control algorithms for reconstructing the shape of an extended elastic inclusion. An original algorithm for finding a good initial guess for

the illuminated part of the elastic inclusion is provided. The algorithm is based on a high-frequency analysis of the MSR matrices and is of migration type. For doing so, one has to decompose the contributions to the MSR matrices of the compressional and shear waves. In section 10, in order to handle topology changes such as breaking one component into two, we convert the optimization procedures into level-set forms. We also formulate a hopping algorithm to improve the reconstruction results using recursively measurements at multiple frequencies. The paper ends with a discussion in section 11. In most of the paper, the MSR matrices are constructed using arrays that enclose the target.

2. Problem formulation. Let μ_0 and ϵ_0 denote the magnetic permeability and electrical permittivity of the background, respectively, that are the electromagnetic parameters in the absence of any inclusion. Suppose that an electromagnetic inclusion D has μ and ϵ as its permeability and permittivity. Throughout this paper, we assume that $\mu_0, \epsilon_0, \mu,$ and ϵ are positive constants.

For a given wavenumber k , let $\Gamma^k(\mathbf{x})$ be the outgoing Green function for $\Delta + k^2$ in $\mathbb{R}^d, d = 2, 3$, corresponding to a Dirac mass at $\mathbf{0}$. That is, Γ^k is the solution to

$$(\Delta + k^2)\Gamma^k(\mathbf{x}) = -\delta_{\mathbf{0}}(\mathbf{x}) \quad \text{in } \mathbb{R}^d,$$

subject to the outgoing radiation condition. In three dimensions, the Green function is given by $\Gamma^k(\mathbf{x}) = e^{ik|\mathbf{x}|}/(4\pi|\mathbf{x}|)$, while in two dimensions, $\Gamma^k(\mathbf{x}) = (i/4)H_0^{(1)}(k|\mathbf{x}|)$, where $H_0^{(1)}$ is the Hankel function of the first kind of order zero.

Suppose that the inclusion D is illuminated by a time-harmonic point source acting at the point $\mathbf{y} \in \mathbb{R}^d \setminus \overline{D}$ at the frequency ω . In this case, the electric field perturbed in the presence of the inclusion is the solution $u(\cdot, \mathbf{y})$ to the transmission problem

$$(2.1) \quad \nabla \cdot \left(\frac{1}{\mu_0} \chi(\mathbb{R}^d \setminus D) + \frac{1}{\mu} \chi(D) \right) \nabla u + \omega^2 \left(\epsilon_0 \chi(\mathbb{R}^d \setminus D) + \epsilon \chi(D) \right) u = -\frac{1}{\mu_0} \delta_{\mathbf{y}}$$

with the radiation condition imposed on u or, equivalently,

$$(2.2) \quad \begin{cases} \Delta u + k_0^2 u = -\delta_{\mathbf{y}} & \text{in } \mathbb{R}^d \setminus \overline{D}, \\ \Delta u + k^2 u = 0 & \text{in } D, \\ u|_+ - u|_- = 0 & \text{on } \partial D, \\ \frac{1}{\mu_0} \frac{\partial u}{\partial \nu} \Big|_+ - \frac{1}{\mu} \frac{\partial u}{\partial \nu} \Big|_- = 0 & \text{on } \partial D, \\ u \text{ satisfies the outgoing radiation condition,} \end{cases}$$

where $k_0 = \omega\sqrt{\epsilon_0\mu_0}$ and $k = \omega\sqrt{\epsilon\mu}$. Here $\partial/\partial\nu$ denotes the normal derivative to ∂D and

$$\frac{\partial u}{\partial \nu} \Big|_{\pm}(\mathbf{x}) := \lim_{t \rightarrow 0^+} \nabla u(\mathbf{x} \pm t\nu) \cdot \nu, \quad \mathbf{x} \in \partial D,$$

if the limits exist.

Suppose that we have coincident transmitter and receiver arrays $\{\mathbf{y}_1, \dots, \mathbf{y}_N\}$ of N elements, used to detect the inclusion. In most of the paper, we use arrays that enclose the target.

In the presence of the inclusion the scattered field induced on the n th receiving element, \mathbf{y}_n , from the scattering of an incident wave generated at \mathbf{y}_m can be expressed as follows:

$$(2.3) \quad A_{nm} = u(\mathbf{y}_n, \mathbf{y}_m) - \Gamma^{k_0}(\mathbf{y}_n - \mathbf{y}_m).$$

By reciprocity the response matrix is complex symmetric (but not Hermitian).

The MSR matrix $\mathbf{A} = (A_{nm})_{n,m=1,\dots,N}$ describes the transmit-receive process performed at the array. The problem we consider is to image the inclusion D from the MSR matrix \mathbf{A} . We assume that the target is extended, i.e., its characteristic size is much larger than half the wavelength, π/k_0 .

Note that the use of the formal equivalence between electromagnetics and linear acoustics, by term-to-term replacing permittivity and permeability by compressibility and volume density of mass, and the electric field by the pressure field, extends the investigation and the results below to acoustics.

3. Optimal control algorithms. Suppose that ϵ and μ are known. Let \mathbf{A}_{meas} denote the measured MSR matrix and let $\mathbf{A}[D]$ be the (computed) MSR matrix associated with the inclusion D . The matrix $\mathbf{A}[D]$ is symmetric by definition, but the measured matrix \mathbf{A}_{meas} may not be symmetric due to an additive noise, for instance. Throughout this paper we symmetrize the measured matrix by the transform $\mathbf{A} \rightarrow (\mathbf{A} + \mathbf{A}^T)/2$. Here T stands for the transpose. As noticed in [6], the symmetrization of the MSR matrix reduces the variance of its off-diagonal entries by a factor of $\sqrt{2}$ in the case of additive noise.

A standard algorithm to image the inclusion is to minimize over D in the class of \mathcal{C}^1 -curves the cost functional defined by [23],

$$(3.1) \quad \mathcal{J}_1[D] := \frac{1}{2} \sum_{n,m=1}^N |A_{nm}[D] - A_{\text{meas},nm}|^2.$$

Throughout this paper, the minimization over the domains is carried out in the class of \mathcal{C}^1 -curves. The parametrization of the domains is a delicate question. Usually, a parametric representation is used. Here, we provide a new representation of shapes in terms of backpropagated significant singular vectors of MSR matrices.

In the following we use extensively the singular value decomposition (SVD) of a symmetric complex matrix \mathbf{A} written in the usual form $\mathbf{A} = \mathbf{V}\mathbf{\Sigma}\bar{\mathbf{V}}^T$. Let $\sigma_{\text{meas}}^{(l)}$, $l = 1, \dots, L$, be the singular values of \mathbf{A}_{meas} counted according to multiplicity and $\mathbf{v}_{\text{meas}}^{(l)}$ be the singular vector associated with $\sigma_{\text{meas}}^{(l)}$, so that $(\mathbf{v}_{\text{meas}}^{(l)})_{l=1}^L$ is a basis of the image space of \mathbf{A}_{meas} , L being its dimension.

A second algorithm is to minimize over D in the class of \mathcal{C}^1 -curves the cost functional defined by

$$(3.2) \quad \mathcal{J}_2[D] := \frac{1}{2} \sum_{l=1}^L W(\sigma_{\text{meas}}^{(l)}) \left\| (\mathbf{A}[D] - \mathbf{A}_{\text{meas}}) \mathbf{v}_{\text{meas}}^{(l)} \right\|^2,$$

where W is a weight function. A weight function is supposed to be a real-valued positive function. As we will see the weight function can be useful to enhance some geometrical

features of the inclusion. Here, the MSR discrepancy is minimized with respect to the signal space.

In this paper we propose a third algorithm. At each step j , we arrange the singular values, $\sigma^{(l')}[D_j]$, of the computed matrix $\mathbf{A}[D_j]$ in descending order and count them according to their multiplicities. Let $\mathbf{v}^{(l')}[D_j]$, $l' = 1, \dots, L'$, be the first L' singular vectors associated with $\sigma^{(l')}[D_j]$. Let $\langle \cdot, \cdot \rangle$ denote the Hermitian product.

A third algorithm is to minimize at the step j over all the changes δD the cost functional

$$(3.3) \quad \mathcal{J}_3^{(j)}[\delta D] := \frac{1}{2} \sum_{l'=1}^{L'} \sum_{l=1}^L W(\sigma_{\text{meas}}^{(l)}) W'(\sigma^{(l')}[D_j]) \left| \left\langle (\mathbf{A}[D_j + \delta D] - \mathbf{A}_{\text{meas}}) \mathbf{v}_{\text{meas}}^{(l)}, \mathbf{v}^{(l')}[D_j] \right\rangle \right|^2,$$

where W' is a second weight function. Here, the MSR discrepancy of the search direction is minimized in the direction of the signal space. Note that the third algorithm is a discrete version of the algorithm introduced in [5]. It is also worth emphasizing that the cost functional $\mathcal{J}_3^{(j)}$ is updated at every step j of the optimization procedure. The first motivation of the third algorithm is to better explore the weakest significant singular values and vectors of the MSR matrix and consequently provide images with high resolution. Second, it uses a natural representation of the shape changes in terms of backpropagation of significant eigenvectors.

In the forthcoming sections, we discuss merits and demerits of these algorithms. We also carry out a detailed stability and resolution analysis in simplified configurations. Using asymptotic formulations of the MSR matrix, we propose a method for choosing a prior guess and show its optimality in the presence of an additive noise in the MSR measurements.

4. Shape derivatives. In order to minimize the cost functional \mathcal{J}_j , $j = 1, 2, 3$, we update ∂D by ∂D^h . To this end we use the shape derivative of the MSR matrix. Let

$$(4.1) \quad \partial D^h := \{ \mathbf{x} + h(\mathbf{x})\boldsymbol{\nu}(\mathbf{x}), \mathbf{x} \in \partial D \},$$

where $\boldsymbol{\nu}$ is the outward unit normal to ∂D and h is a C^1 function on ∂D . Let the polarization tensor

$$\mathbf{M} \begin{bmatrix} \mu_0 \\ \mu \end{bmatrix} (\mathbf{x}) = \left(\frac{\mu_0}{\mu} - 1 \right) \left(\frac{\mu_0}{\mu} \boldsymbol{\nu}(\mathbf{x}) \otimes \boldsymbol{\nu}(\mathbf{x}) + \boldsymbol{\tau}(\mathbf{x}) \otimes \boldsymbol{\tau}(\mathbf{x}) \right), \quad \mathbf{x} \in \partial D,$$

in two dimensions, where $\boldsymbol{\tau}(\mathbf{x})$ is the unit tangential vector to ∂D at \mathbf{x} , and

$$\mathbf{M} \begin{bmatrix} \mu_0 \\ \mu \end{bmatrix} (\mathbf{x}) = \left(\frac{\mu_0}{\mu} - 1 \right) \left(\frac{\mu_0}{\mu} \boldsymbol{\nu}(\mathbf{x}) \otimes \boldsymbol{\nu}(\mathbf{x}) + \sum_{k=1}^2 \boldsymbol{\tau}_k(\mathbf{x}) \otimes \boldsymbol{\tau}_k(\mathbf{x}) \right), \quad \mathbf{x} \in \partial D,$$

in the three-dimensional case, where $\boldsymbol{\tau}_1(\mathbf{x})$ and $\boldsymbol{\tau}_2(\mathbf{x})$ are two orthogonal unit tangential vectors to ∂D at \mathbf{x} . The polarization tensors are diagonal matrices in the normal, tangential basis associated with ∂D .

Let $u[D](\mathbf{x}, \mathbf{y})$ be the solution to (2.2). The following asymptotic formula holds as $\|h\|_{C^1} \rightarrow 0$:

$$(4.2) \quad u[D^h](\mathbf{x}, \mathbf{y}) - u[D](\mathbf{x}, \mathbf{y}) = \int_{\partial D} h(\mathbf{z}) \left[\nabla_{\mathbf{z}} u[D](\mathbf{x}, \mathbf{z})^T \mathbf{M} \begin{bmatrix} \mu_0 \\ \mu \end{bmatrix} (\mathbf{z}) \nabla_{\mathbf{z}} u[D](\mathbf{z}, \mathbf{y}) + \omega^2(\epsilon - \epsilon_0) \mu_0 u[D](\mathbf{x}, \mathbf{z}) u[D](\mathbf{z}, \mathbf{y}) \right] d\sigma(\mathbf{z}) + o(\|h\|_{C^1})$$

for \mathbf{x} away from D . Formula (4.2) can be proved in exactly the same way as in [13]; see [2] and [10]. Therefore, we have (using the reciprocity $u(\mathbf{x}, \mathbf{y}) = u(\mathbf{y}, \mathbf{x})$)

$$(4.3) \quad \begin{aligned} A_{nm}[D^h] - A_{nm}[D] &= \int_{\partial D} h(\mathbf{x}) \left[\nabla_{\mathbf{x}} u[D](\mathbf{x}, \mathbf{y}_n)^T \mathbf{M} \begin{bmatrix} \mu_0 \\ \mu \end{bmatrix} (\mathbf{x}) \nabla_{\mathbf{x}} u[D](\mathbf{x}, \mathbf{y}_m) \right. \\ &\quad \left. + \omega^2(\epsilon - \epsilon_0)\mu_0 u[D](\mathbf{x}, \mathbf{y}_n)u[D](\mathbf{x}, \mathbf{y}_m) \right] d\sigma(\mathbf{x}) + o(\|h\|_{C^1}). \end{aligned}$$

Let $\mathbf{B}[D](\mathbf{x}) = (B_{nm}[D](\mathbf{x}))_{n,m=1}^N$ be the matrix defined by

$$(4.4) \quad \begin{aligned} B_{nm}[D](\mathbf{x}) &:= \nabla_{\mathbf{x}} u[D](\mathbf{x}, \mathbf{y}_n)^T \mathbf{M} \begin{bmatrix} \mu_0 \\ \mu \end{bmatrix} (\mathbf{x}) \nabla_{\mathbf{x}} u[D](\mathbf{x}, \mathbf{y}_m) \\ &\quad + \omega^2(\epsilon - \epsilon_0)\mu_0 u[D](\mathbf{x}, \mathbf{y}_n)u[D](\mathbf{x}, \mathbf{y}_m). \end{aligned}$$

Note that \mathbf{B} depends not only on D but also on ω and on the contrasts μ_0/μ and ϵ_0/ϵ . Note also that the matrix \mathbf{B} is a propagator since \mathbf{B} applied to a vector data corresponds to propagating the data up the boundary ∂D .

Now, for a cost functional \mathcal{J} , define its shape derivative by

$$(d_S \mathcal{J}[D], h) = \lim_{\delta \rightarrow 0} \frac{\mathcal{J}[D^{\delta h}] - \mathcal{J}[D]}{\delta},$$

where $D^{\delta h}$ is defined as in (4.1) with h replaced by δh . From (4.3) it follows that the shape derivatives of the cost functionals $\mathcal{J}_j, j = 1, 2, 3$, are given by

$$\begin{aligned} (d_S \mathcal{J}_1[D], h) &= \sum_{n,m=1}^N \operatorname{Re} \left[(A_{nm}[D] - A_{\text{meas},nm}) \int_{\partial D} h \overline{B_{nm}[D]} d\sigma \right], \\ (d_S \mathcal{J}_2[D], h) &= \operatorname{Re} \sum_{l=1}^L W(\sigma_{\text{meas}}^{(l)}) \int_{\partial D} h \left\langle (\mathbf{A}[D] - \mathbf{A}_{\text{meas}}) \mathbf{v}_{\text{meas}}^{(l)}, \mathbf{B}[D] \mathbf{v}_{\text{meas}}^{(l)} \right\rangle d\sigma, \\ (d_S \mathcal{J}_3^{(j)}[D_j], h) &= \operatorname{Re} \sum_{l'=1}^{L'} \sum_{l=1}^L W(\sigma_{\text{meas}}^{(l)}) W'(\sigma^{(l')}[D_j]) \left\langle (\mathbf{A}[D_j] - \mathbf{A}_{\text{meas}}) \mathbf{v}_{\text{meas}}^{(l)}, \mathbf{v}^{(l')}[D_j] \right\rangle \\ &\quad \times \int_{\partial D} h \overline{\left\langle \mathbf{B}[D_j] \mathbf{v}_{\text{meas}}^{(l)}, \mathbf{v}^{(l')}[D_j] \right\rangle} d\sigma. \end{aligned}$$

Therefore, we look for the changes h in the first, second, and third algorithms in the vector spaces spanned by $\{\psi_p\}$ defined as, respectively,

$$\begin{aligned} \{\psi_p\} &= \{\operatorname{Re}(B_{nm}[D])\}_{n,m=1}^N \cup \{\operatorname{Im}(B_{nm}[D])\}_{n,m=1}^N, \\ \{\psi_p\} &= \{\operatorname{Re}\langle (\mathbf{A}[D] - \mathbf{A}_{\text{meas}}) \mathbf{v}_{\text{meas}}^{(l)}, \mathbf{B}[D] \mathbf{v}_{\text{meas}}^{(l)} \rangle\}, \\ \{\psi_p\} &= \{\operatorname{Re}\langle \mathbf{B}[D_j] \mathbf{v}_{\text{meas}}^{(l)}, \mathbf{v}^{(l')}[D_j] \rangle\} \cup \{\operatorname{Im}\langle \mathbf{B}[D_j] \mathbf{v}_{\text{meas}}^{(l)}, \mathbf{v}^{(l')}[D_j] \rangle\}. \end{aligned}$$

Moreover, in the m th algorithm, $m = 1, 2, 3$, we modify at each step j ∂D_j to obtain $\partial D_{j+1} := \partial D^{h_j}$ by applying the gradient descent method [26], where $\partial D^{h_j} := \{\mathbf{x} + h_j(\mathbf{x})\boldsymbol{\nu}(\mathbf{x}), \mathbf{x} \in \partial D_j\}$.

For doing so, we choose h_j as follows:

$$(4.5) \quad h_j[\omega](\mathbf{x}) = -\frac{\mathcal{J}_m[D_j]}{\sum_l |(d_S \mathcal{J}_m[D_j], \psi_l)|^2} \sum_l (d_S \mathcal{J}_m[D_j], \psi_l) \psi_l.$$

In the case where $\mathcal{J}_m[D_{j+1}] \geq \mathcal{J}_m[D_j]$ we choose the descent step length by Armijo's rule [26]. We replace h_j by $h_j/2^s$, where s is the smallest integer such that $\mathcal{J}_m[D^{h_j/2^s}] < \mathcal{J}_m[D_j]$; $\partial D^{h_j/2^s} := \{\mathbf{x} + h_j(\mathbf{x})/2^s \boldsymbol{\nu}(\mathbf{x}), \mathbf{x} \in \partial D_j\}$.

If we have measurements of the MSR matrix at multiple frequencies $(\omega_p)_{p=1, \dots, P}$, then the change in the step j is given by

$$(4.6) \quad h_j(\mathbf{x}) = \frac{1}{P} \sum_{p=1}^P h_j[\omega_p](\mathbf{x}).$$

We also note that in the third algorithm the higher L' is, the better the resolution, which is quite natural. However, for a finite signal-to-noise ratio in the measurements, large L' leads to an unstable reconstruction. As will be seen later, there is a trade-off between the resolution and the stability.

5. The Born approximation in the nonmagnetic case. In this section we assume $\mu = \mu_0$ and address the case where the Born approximation is valid. We consider a circular geometry with target in the center. This configuration allows us to do a detailed resolution and stability analysis in the presence of an additive measurement noise. This analysis is also useful for choosing the prior guess in the imaging functional as shown in section 7. In connection with our results, we refer to [32, 22] for the design of direct imaging procedures within the Born approximation.

5.1. Asymptotic formulation of the response matrix. Let D_{true} be the true inclusion. If we set $\mu = \mu_0$ and $\epsilon \approx \epsilon_0$, then by using the Born approximation

$$u[D_{\text{true}}](\mathbf{x}, \mathbf{y}_n) \approx \Gamma^{k_0}(\mathbf{x} - \mathbf{y}_n) \quad \forall 1 \leq n \leq N \quad \text{and} \quad \mathbf{x} \in D_{\text{true}}.$$

Therefore, we have

$$A_{\text{meas}, nm} \approx \omega^2(\epsilon - \epsilon_0)\mu_0 \int_{D_{\text{true}}} \Gamma^{k_0}(\mathbf{x} - \mathbf{y}_n) \Gamma^{k_0}(\mathbf{x} - \mathbf{y}_m) d\mathbf{x}.$$

If we define the matrix

$$\mathbf{B}[\omega](\mathbf{x}) := \left(\Gamma^{k_0}(\mathbf{x} - \mathbf{y}_n) \Gamma^{k_0}(\mathbf{x} - \mathbf{y}_m) \right)_{n,m=1}^N \quad \text{for } \mathbf{x} \in D_{\text{true}},$$

then we can write

$$\mathbf{A}_{\text{meas}} \approx \omega^2(\epsilon - \epsilon_0)\mu_0 \int_{D_{\text{true}}} \mathbf{B}[\omega](\mathbf{x}) d\mathbf{x}.$$

Note that in this case \mathbf{B} does not depend on D_{true} . Below we assume $d = 2$. If ω is large, then

$$\mathbf{B}[\omega](\mathbf{x}) \approx \frac{i}{8\pi k_0} \left(\frac{e^{ik_0(|\mathbf{x}-\mathbf{y}_n|+|\mathbf{x}-\mathbf{y}_m|)}}{\sqrt{|\mathbf{x}-\mathbf{y}_n||\mathbf{x}-\mathbf{y}_m|}} \right)_{n,m}.$$

Assuming further that the distance L_F between the array and the target is much larger than the aperture yields

$$\mathbf{B}[\omega](\mathbf{x}) \approx \frac{i}{8\pi k_0 L_F} \left(e^{ik_0(|\mathbf{x}-\mathbf{y}_n|+|\mathbf{x}-\mathbf{y}_m|)} \right)_{n,m}.$$

In polar coordinates, let the points of the array be

$$\mathbf{y}_n = (R_n \cos \theta_n, R_n \sin \theta_n),$$

and let the domain D_{true} be of the form

$$(5.1) \quad D_{\text{true}} = \{ \mathbf{y} = (r \cos \theta, r \sin \theta), 0 \leq r \leq R(\theta), 0 \leq \theta \leq 2\pi \}.$$

Using the Taylor series expansion

$$(5.2) \quad |\mathbf{y}_n - \mathbf{x}| = |\mathbf{y}_n| - \frac{\mathbf{y}_n \cdot \mathbf{x}}{|\mathbf{y}_n|} + O\left(\frac{|\mathbf{x}|^2}{|\mathbf{y}_n|}\right),$$

we find that in polar coordinates $\mathbf{x} = (r \cos \theta, r \sin \theta)$,

$$A_{\text{meas},mn}[D_{\text{true}}] = e^{ik_0[R_n+R_m]} \int_0^{2\pi} d\theta \int_0^{R(\theta)} r dr e^{-ik_0r[\cos(\theta-\theta_m)+\cos(\theta-\theta_n)]},$$

up to a multiplicative constant, which is valid if $k_0 \text{diam}^2(D)$ is much smaller than the distance from the target D to the array (this is the Fraunhofer regime).

Note that the first phase factor in the response matrix does not modify the singular values and it modifies the singular vectors only by a phase term independent of the singular value itself. In the following this factor is removed.

5.1.1. The unperturbed domain. We assume in this subsection that the domain $D_{\text{true}} := D_0$, a disk with radius r_0 . In the continuum approximation (the number of array elements $N \rightarrow +\infty$) the response matrix is proportional to the operator whose kernel is

$$\mathcal{A}[D_0](\theta_1, \theta_2) = \frac{1}{\pi r_0^2} \int_0^{2\pi} d\theta \int_0^{r_0} r dr e^{-ik_0r[\cos(\theta-\theta_1)+\cos(\theta-\theta_2)]}.$$

The kernel can be written as [1, Formulas 9.1.21 and 9.1.30]

$$\mathcal{A}[D_0](\theta_1, \theta_2) = a(\theta_1 - \theta_2) \text{ with } a(\theta) = 2 \frac{J_1(2k_0r_0 \cos(\frac{\theta}{2}))}{2k_0r_0 \cos(\frac{\theta}{2})}.$$

The function $a(\theta)$ can be expanded in Fourier series as [1, Formula 11.4.7]

$$a(\theta) = \sum_{n=-\infty}^{\infty} \hat{a}_n e^{in\theta} \text{ with } \hat{a}_n = (-1)^n (J_n^2 - J_{n-1}J_{n+1})(k_0r_0),$$

where J_n is the Bessel function of the first kind of order n , which shows that the singular values of $\mathcal{A}[D_0]$ are $(\sqrt{2\pi}|\hat{a}_p|)_{p \in \mathbb{N}}$, each of which (except $\sqrt{2\pi}|\hat{a}_0|$) is of multiplicity two. The

associated singular vectors are $(\psi^{(p,\pm)}(\theta))_{\theta \in [0,2\pi]} = (e^{\pm ip\theta} / \sqrt{2\pi})_{\theta \in [0,2\pi]}$. Moreover, in the asymptotic framework $k_0 r_0 \gg 1$, there are about $2k_0 r_0$ significant singular values. More exactly, using [1, Formula 9.3.3], we find that for $k_0 r_0 \gg 1$ and $n \in [-k_0 r_0, k_0 r_0]$,

$$|\hat{a}_n| \simeq \frac{2}{\pi k_0 r_0} \sqrt{1 - \left(\frac{n}{k_0 r_0}\right)^2}.$$

For $k_0 r_0 \gg 1$ and $|n| > k_0 r_0$ the singular values are exponentially small. See, for instance, [16, 17].

5.1.2. The perturbed domain. We assume in this subsection that the domain D_{true} is a deformed disk (around the perfect disk D_0 with radius r_0). In polar coordinates $\mathbf{x} = (r \cos \theta, r \sin \theta)$ the domain D_{true} is given by (5.1) with

$$(5.3) \quad R(\theta) = r_0 + h_{\text{true}}(\theta), \quad h_{\text{true}}(\theta) = \sum_{p=-\infty}^{\infty} \hat{h}_{\text{true},p} e^{ip\theta}.$$

We address the regime in which $k_0 \|h_{\text{true}}\|_{\infty} \ll 1 < k_0 r_0$. In the continuum approximation the perturbation of the response matrix is the operator with the kernel

$$\begin{aligned} \mathcal{H}[D_{\text{true}}](\theta_1, \theta_2) &:= \mathcal{A}[D_{\text{true}}](\theta_1, \theta_2) - \mathcal{A}[D_0](\theta_1, \theta_2) \\ &\approx \frac{1}{\pi r_0} \int_0^{2\pi} d\theta h_{\text{true}}(\theta) e^{-ik_0 r_0 [\cos(\theta - \theta_1) + \cos(\theta - \theta_2)]}. \end{aligned}$$

The results of the previous subsection indicate that we should represent the perturbation of the response matrix in the Fourier domain, since the singular vectors of the unperturbed response matrix are the Fourier modes. The Fourier coefficients of the kernel of the operator $\mathcal{H}[D_{\text{true}}]$ are defined by

$$\hat{\mathcal{H}}_{jl}[D_{\text{true}}] = \frac{1}{(2\pi)^2} \int \mathcal{H}[D_{\text{true}}](\theta_1, \theta_2) e^{-ij\theta_1 - il\theta_2} d\theta_1 d\theta_2,$$

and they are given by

$$\hat{\mathcal{H}}_{jl}[D_{\text{true}}] = \frac{2}{r_0} \hat{h}_{\text{true},j+l} J_j(k_0 r_0) J_l(k_0 r_0) i^{-j-l}.$$

5.2. Resolution and stability analysis of the imaging functionals. Assuming measurement noise, we perform a resolution and stability analysis of the proposed algorithms. We assume that the receiver-transmitter array covers in a dense manner a closed surface surrounding the inclusion D .

We assume that the domain is the deformed disk D_{true} given by (5.3) and that the response matrix is corrupted by an additive Gaussian white noise $\varepsilon_{\text{meas}}$ or, equivalently, in the continuum approximation the kernel of the operator is given by

$$\mathcal{A}_{\text{meas}}(\theta_1, \theta_2) = \mathcal{A}[D_{\text{true}}](\theta_1, \theta_2) + \varepsilon_{\text{meas}}(\theta_1, \theta_2).$$

The purpose of the imaging process is to estimate the function $h_{\text{true}}(\theta)$ that characterizes D_{true} . The results of the previous subsection indicate that we should look for the Fourier coefficients $(\hat{h}_{\text{true},p})_{p \in \mathbb{Z}}$ that characterize the boundary of the domain D_{true} .

5.2.1. First functional. The first imaging functional defined in (3.1) is

$$\mathcal{J}_1[D] = \frac{1}{2} \|\mathcal{A}[D](\cdot, \cdot) - \mathcal{A}_{\text{meas}}(\cdot, \cdot)\|_2^2 = \frac{1}{2} \|\mathcal{H}[D](\cdot, \cdot) - \mathcal{H}[D_{\text{true}}](\cdot, \cdot) - \varepsilon_{\text{meas}}(\cdot, \cdot)\|_2^2.$$

Here $\|\cdot\|_2$ denotes the L^2 norm. The domain D is characterized by the function $(h(\theta))_{\theta \in [0, 2\pi]}$. Using Parseval's formula the first imaging functional can be written as

$$\mathcal{J}_1[D] = \frac{(2\pi)^2}{2} \sum_{l', l = -\infty}^{\infty} |(\mathcal{Q}_1 \hat{h})_{l'} - (\mathcal{Q}_1 \hat{h}_{\text{true}})_{l'} - \hat{\varepsilon}_{\text{meas}, l'}|^2,$$

where $\hat{\varepsilon}_{\text{meas}, l'}$ are the Fourier coefficients of $\varepsilon_{\text{meas}}(\cdot, \cdot)$ and

$$(\mathcal{Q}_1 \hat{h})_{l'} = \frac{2}{r_0} \hat{h}_{l'+l} J_{l'}(k_0 r_0) J_l(k_0 r_0) i^{-l'-l}, \quad l', l \in \mathbb{Z}.$$

The least-square inverse is

$$((\mathcal{Q}_1^* \mathcal{Q}_1)^{-1} \mathcal{Q}_1^* \hat{\varepsilon})_p = \frac{r_0 \sum_{l=-\infty}^{\infty} J_l(k_0 r_0) J_{p-l}(k_0 r_0) i^p \hat{\varepsilon}_{l, p-l}}{2 \sum_{l=-\infty}^{\infty} J_l^2(k_0 r_0) J_{p-l}^2(k_0 r_0)}, \quad p \in \mathbb{Z}.$$

Therefore, given the measured kernel $\mathcal{A}_{\text{meas}}$, the least-square estimation $(\hat{h}_{\text{est}, p})_{p \in \mathbb{Z}}$ of the Fourier coefficients of the shape $h_{\text{true}}(\theta)$ of the domain D_{true} is

$$(\hat{h}_{\text{est}, p})_{p \in \mathbb{Z}} = (\mathcal{Q}_1^* \mathcal{Q}_1)^{-1} \mathcal{Q}_1^* ((\hat{\mathcal{A}}_{\text{meas}, l'} - \hat{\mathcal{A}}_{l'}(D_0))_{l', l \in \mathbb{Z}}).$$

This gives, for all $p \in \mathbb{Z}$,

$$\hat{h}_{\text{est}, p} = \hat{h}_{\text{true}, p} + \frac{r_0 \sum_{l=-\infty}^{\infty} J_l(k_0 r_0) J_{p-l}(k_0 r_0) i^p \hat{\varepsilon}_{\text{meas}, l, p-l}}{2 \sum_{l=-\infty}^{\infty} J_l^2(k_0 r_0) J_{p-l}^2(k_0 r_0)},$$

which shows that the estimation is unbiased with the variance

$$\text{Var}(\hat{h}_{\text{est}, p}) = \frac{r_0^2 \sigma^2}{4 \sum_{l=-\infty}^{\infty} J_l^2(k_0 r_0) J_{p-l}^2(k_0 r_0)},$$

where $\sigma^2 = \mathbb{E}(|\hat{\varepsilon}_{\text{meas}, l'}|^2)$ (independent on l', l for white noise). Here \mathbb{E} stands for the expectation (mean value).

Now, from Neumann's formula [19, Formula 7.7.2(11)], we have for any $l \in \mathbb{Z}$

$$J_l(k_0 r_0) J_{p-l}(k_0 r_0) = \frac{1}{2\pi} \int_0^{2\pi} J_p(2k_0 r_0 \cos \theta) \cos((2l - p)\theta) d\theta.$$

Using Parseval's formula gives

$$\sum_{l=-\infty}^{\infty} J_l^2(k_0 r_0) J_{p-l}^2(k_0 r_0) = \frac{1}{2\pi} \int_0^{2\pi} J_p^2(2k_0 r_0 \cos \theta) d\theta.$$

It follows from [31, Equation (4)] that in the asymptotic framework when $k_0r_0 \gg 1$ and p is smaller than $2k_0r_0$,

$$\sum_{l=-\infty}^{\infty} J_l^2(k_0r_0)J_{p-l}^2(k_0r_0) \sim \frac{1}{\pi^2k_0r_0} \left[\log k_0r_0 + 5 \ln 2 + \gamma - 2 \left(1 + \frac{1}{3} + \dots + \frac{1}{2p-1} \right) + O\left(\frac{1}{(k_0r_0)^{1/2}}\right) \right],$$

where γ is the Euler’s constant, while when p is larger than $2k_0r_0$ the sum is exponentially close to zero. We can therefore conclude that in the presence of a small additive noise,

- (i) the estimation of $\hat{h}_{\text{true},p}$ is possible for $p < 2k_0r_0$ with the accuracy (standard deviation) of the order of $(\sigma_{r_0}/2)\pi(k_0r_0)^{1/2}/\log^{1/2}(k_0r_0)$ and impossible for $p > 2k_0r_0$;
- (ii) the coefficient \hat{h}_p corresponds to a feature at the surface of the unperturbed disk D_0 whose characteristic length scale is $2\pi r_0/p$, and therefore the limitation $p < 2k_0r_0$ corresponds to a length scale larger than half a wavelength, which is the diffraction limit.

5.2.2. The second functional. The second imaging functional defined in (3.2) is

$$\begin{aligned} \mathcal{J}_2[D] &= \frac{1}{2} \sum_{l=1}^{2L+1} W(\sigma_{\text{meas}}^{(l)}) \|(\mathcal{A}[D](\cdot, \cdot) - \mathcal{A}_{\text{meas}}(\cdot, \cdot))v_{\text{meas}}^{(l)}(\cdot)\|_2^2 \\ &= \frac{1}{2} \sum_{l=1}^{2L+1} W(\sigma_{\text{meas}}^{(l)}) \|(\mathcal{H}[D](\cdot, \cdot) - \mathcal{H}[D_{\text{true}}](\cdot, \cdot) - \varepsilon_{\text{meas}}(\cdot, \cdot))v_{\text{meas}}^{(l)}(\cdot)\|_2^2, \end{aligned}$$

where $\sigma_{\text{meas}}^{(l)}$ and $v_{\text{meas}}^{(l)}$ are the l th singular value and singular vector of $\mathcal{A}_{\text{meas}}$. If D_{true} is a small deformation of the disk D_0 and the additive white noise is small, then the difference between the singular vectors of $\mathcal{A}_{\text{meas}}$ and those of $\mathcal{A}[D_0]$ is small, and therefore, after relabeling the vectors and up to an error that is of higher order, we have

$$\mathcal{J}_2[D] = \frac{1}{2} \sum_{l=-L}^L w_l \|(\mathcal{H}[D](\cdot, \cdot) - \mathcal{H}[D_{\text{true}}](\cdot, \cdot) - \varepsilon_{\text{meas}}(\cdot, \cdot))\psi^{(l)}(\cdot)\|_2^2,$$

where $\psi^{(l)}(\theta) = e^{i\theta}/\sqrt{2\pi}$ and $w_l = W(\sigma_{|l|}) = W((J_l^2 - J_{l-1}J_{l+1})(k_0r_0))$. We have

$$(\mathcal{H}[D]\psi^{(l)})(\theta) = \frac{2\sqrt{2\pi}}{r_0} \sum_p \hat{h}_p J_{l+p}(k_0r_0)J_l(k_0r_0)i^{-2l-p}e^{i(l+p)\theta}.$$

Using Parseval’s formula, we get

$$\mathcal{J}_2[D] = \frac{(2\pi)^2}{2} \sum_{l'=-\infty}^{\infty} \sum_{l=-L}^L w_l |(\mathcal{Q}_2\hat{h})_{l'l} - (\mathcal{Q}_2\hat{h}_{\text{true}})_{l'l} - \hat{\varepsilon}_{\text{meas},l'l}|^2,$$

where

$$(\mathcal{Q}_2\hat{h})_{l'l} = \frac{2}{r_0} \hat{h}_{l'+l} J_{l'}(k_0r_0)J_l(k_0r_0)i^{-(l'+l)}, \quad l' \in \mathbb{Z}, \quad l = -L, \dots, L.$$

Introducing the multiplication operator \mathcal{W}_2 defined by

$$(\mathcal{W}_2 \hat{\varepsilon})_{l'l} = w_l \hat{\varepsilon}_{l'l}, \quad l' \in \mathbb{Z}, \quad l = -L, \dots, L,$$

the least-square inverse is

$$((\mathcal{Q}_2^* \mathcal{W}_2 \mathcal{Q}_2)^{-1} \mathcal{Q}_2^* \mathcal{W}_2 \hat{\varepsilon})_p = \frac{r_0 \sum_{l=-L}^L w_l J_l(k_0 r_0) J_{p+l}(k_0 r_0) i^{p+2l} \hat{\varepsilon}_{p+l, -l}}{2 \sum_{l=-L}^L w_l (J_l(k_0 r_0) J_{p+l}(k_0 r_0))^2}, \quad p \in \mathbb{Z}.$$

Therefore the least-square estimation $(\hat{h}_{\text{est}, p})_{p \in \mathbb{Z}}$ of the Fourier coefficients of the shape $h_{\text{true}}(\theta)$ of the domain D_{true} is

$$(\hat{h}_{\text{est}, p})_{p \in \mathbb{Z}} = ((\mathcal{Q}_2^* \mathcal{W}_2 \mathcal{Q}_2)^{-1} \mathcal{Q}_2^* \mathcal{W}_2 ((\hat{\mathcal{A}}_{\text{meas}, l'l} - \hat{\mathcal{A}}_{l'l}[D_0])_{l' \in \mathbb{Z}, l = -L, \dots, L})).$$

This gives, for all $p \in \mathbb{Z}$,

$$\hat{h}_{\text{est}, p} = \hat{h}_{\text{true}, p} + \frac{r_0 \sum_{l=-L-p}^{L-p} w_{l+p} J_l(k_0 r_0) J_{p-l}(k_0 r_0) i^p \hat{\varepsilon}_{\text{meas}, l, p+l}}{2 \sum_{l=-L}^L w_l J_l^2(k_0 r_0) J_{p-l}^2(k_0 r_0)},$$

which implies that the estimation is unbiased with the variance

$$\text{Var}(\hat{h}_{\text{est}, p}) = \frac{r_0^2 \sigma^2}{4} \frac{\sum_{l=-L}^L w_l^2 J_l^2(k_0 r_0) J_{p-l}^2(k_0 r_0)}{[\sum_{l=-L}^L w_l J_l^2(k_0 r_0) J_{p-l}^2(k_0 r_0)]^2}.$$

It is natural to look for the optimal weight function W , that is, the one that minimizes the variance. The minimization problem can be solved using Lagrange multipliers, and one finds that W should be constant. This result shows that the optimal weight function for the second functional is the uniform weight in the presence of white noise. This is characteristic of the situation addressed in this section, in which the array surrounds the target and the Born approximation holds true, which implies that illumination should be uniform (in the angle space). As we will see in section 6.2, weighting can become important when these ideal conditions are not fulfilled.

When the weight function W is constant, then the variance of the estimation is

$$\text{Var}(\hat{h}_{\text{est}, p}) = \frac{\sigma^2 r_0^2}{4 \sum_{l=-L}^L J_l^2(k_0 r_0) J_{p-l}^2(k_0 r_0)}.$$

This result shows that the second functional is more sensitive to an additive white noise than the first one for small L , while they are equivalent when $L > k_0 r_0$. If the noise is colored (which is the case when the noise comes from random heterogeneities in the medium), then the situation can be more complex.

Note that these conclusions hold because of the continuum approximation. However, in the discrete case when there is only a finite number of transmitters and receivers, as will be seen later, method 2 is better than method 1 since the information in the noise space is filtered out.

5.2.3. The third functional. The third imaging functional defined in (3.3) (for $j = 0$) is

$$\mathcal{J}_3[D] = \frac{1}{2} \sum_{l'=1}^{2L'+1} \sum_{l=1}^{2L+1} W(\sigma_{\text{meas}}^{(l)}) W'(\sigma^{(l')}[D_0]) \left| \left\langle (\mathcal{A}[D] - \mathcal{A}_{\text{meas}}) v_{\text{meas}}^{(l)}, v^{(l')}[D_0] \right\rangle \right|^2.$$

To leading order in the amplitude of the noise and the deformation of the domain, we have after relabeling the vectors

$$\mathcal{J}_3[D] = \frac{1}{2} \sum_{l=-L}^L \sum_{l'=-L'}^{L'} w_l w_{l'} \left| \left\langle (\mathcal{H}[D] - \mathcal{H}[D_{\text{true}}] - \varepsilon_{\text{meas}}) \psi^{(l)}, \psi^{(l')} \right\rangle \right|^2$$

with $w_l = W(\sigma_{|l|}) = W((J_l^2 - J_{l-1} J_{l+1})(k_0 r_0))$ and $w_{l'} = W'(\sigma_{|l'|})$. Using Parseval’s formula, we get

$$\mathcal{J}_3[D] = \frac{(2\pi)^2}{2} \sum_{l'=-L'}^{L'} \sum_{l=-L}^L w_l w_{l'} \left| (\mathcal{Q}_3 \hat{h})_{l'l} - (\mathcal{Q}_3 \hat{h}_{\text{true}})_{l'l} - \hat{\varepsilon}_{\text{meas},l',-l} \right|^2,$$

where

$$(\mathcal{Q}_3 \hat{h})_{l'l} = \frac{2}{r_0} \hat{h}_{l'-l} J_{l'}(k_0 r_0) J_l(k_0 r_0) i^{-l'-l}, \quad l' = -L', \dots, L', \quad l = -L, \dots, L.$$

Note that $\mathcal{Q}_3 \hat{h}$ is a function of $(\hat{h}_p)_{p=-L-L', L+L'}$ only. Denoting by \mathcal{W}_3 the multiplication operator

$$(\mathcal{W}_3 \varepsilon)_{l'l} = w_{l'} w_l \varepsilon_{l'l}, \quad l' = -L', \dots, L', \quad l = -L, \dots, L,$$

the least-square estimation $(\hat{h}_{\text{est},p})_{p=-L-L', \dots, L+L'}$ of the first Fourier coefficients of the shape $h_{\text{true}}(\theta)$ of the domain D_{true} is

$$(\hat{h}_{\text{est},p})_{p=-L-L', \dots, L+L'} = (\mathcal{Q}_3^* \mathcal{W}_3 \mathcal{Q}_3)^{-1} \mathcal{Q}_3^* \mathcal{W}_3 ((\hat{\mathcal{A}}_{\text{meas},l'l} - \hat{\mathcal{A}}_{l'l}[D_0])_{l'=-L', \dots, L', l=-L, \dots, L}).$$

This gives, for all $p = -L - L', \dots, L + L'$,

$$\hat{h}_{\text{est},p} = \hat{h}_{\text{true},p} + \frac{r_0 \sum_{l=-L \vee -L'+p}^{L \wedge L'+p} J_l(k_0 r_0) J_{p-l}(k_0 r_0) i^p \hat{\varepsilon}_{\text{meas},l,p-l}}{2 \sum_{l=-L \vee -L'+p}^{L \wedge L'+p} (J_l(k_0 r_0) J_{p-l}(k_0 r_0))^2},$$

which implies that the estimation is unbiased with the variance

$$\text{Var}(\hat{h}_{\text{est},p}) = \frac{\sigma^2 r_0^2}{4 \sum_{l=-L \vee -L'+p}^{L \wedge L'+p} (J_l(k_0 r_0) J_{p-l}(k_0 r_0))^2}.$$

This result shows that it is possible to reconstruct the Fourier coefficients \hat{h}_p up to $p = (L + L') \wedge 2k_0 r_0$ using the third functional. Here $a \wedge b$ and $a \vee b$, respectively, denote the minimum and the maximum between a and b .

In this section we have chosen a particular geometry so as to be able to carry out a detailed resolution and stability analysis. It should be possible to carry out such detailed analysis in

different geometries. For instance, if the array has finite aperture and covers only an angular cone with angular width $\theta_a \ll 2\pi$, then it should be possible to express the singular vectors in terms of prolate spheroidal functions [17, 20] and to use asymptotic results of the singular value distribution for the sinc kernel [25, 30]. The analysis should then be similar to the one carried out in section 6 and should lead to the conclusion that it is possible to reconstruct the shape of the inclusion with a resolution of the order of the Rayleigh resolution formula $(2\pi/\theta_a)(\pi/k_0)$. The case in which the continuum approximation is not valid (which means that there is only a finite number of transmitters and receivers and the interdistance between the sensors is large) is also of interest but its analysis is more complicated. Numerical simulations may be the right tool to study such situations.

Note also because of the continuum approximation and the simplicity of the configuration considered here, weighting plays no role. As we will see in the next sections, it can become important when the ideal conditions assumed here are not fulfilled.

6. Asymptotic formulation in the case of both permittivity and permeability contrasts.

Now we turn to the general case of both permittivity and permeability contrasts, that is, without assuming Born approximation. As in the case where the Born approximation is valid, we carry out a (formal) high-frequency asymptotic analysis of the MSR matrix. We use such high-frequency asymptotic analysis to derive a method for constructing a good initial guess. We also make use of it in order to connect the eigenvalues and the eigenvectors of the MSR matrix to the target shape and give a detailed resolution analysis in a simplified configuration.

6.1. High-frequency asymptotics of the response matrix. Write

$$u[D](\mathbf{x}, \mathbf{y}_n) = \begin{cases} \Gamma^{k_0}(\mathbf{x} - \mathbf{y}_n) + u_n^{(s)}(\mathbf{x}) & \text{for } \mathbf{x} \in \mathbb{R}^2 \setminus \bar{D}, \\ u_n^{(t)}(\mathbf{x}) & \text{for } \mathbf{x} \in D. \end{cases}$$

Using Green’s formula, we get

$$A_{nm}[D, \omega] = \int_{\partial D} \left(\frac{\partial \Gamma^{k_0}}{\partial \nu}(\mathbf{y}_m - \mathbf{x})u_n^{(s)}(\mathbf{x}) - \Gamma^{k_0}(\mathbf{y}_m - \mathbf{x})\frac{\partial u_n^{(s)}}{\partial \nu}(\mathbf{x}) \right) d\sigma(\mathbf{x}).$$

Using a WKB approximation for $u_n^{(s)}$ and $\frac{\partial u_n^{(s)}}{\partial \nu}$ on ∂D as $\omega \rightarrow +\infty$ [24], we find the high-frequency asymptotic expansion

$$(6.1) \quad u_n^{(s)}(\mathbf{x}) \approx a_n^{(s)}(\mathbf{x}) \frac{e^{ik_0|\mathbf{x}-\mathbf{y}_n|}}{\sqrt{|\mathbf{x}-\mathbf{y}_n|}} \quad \text{and} \quad \frac{\partial u_n^{(s)}}{\partial \nu}(\mathbf{x}) \approx -ik_0 a_n^{(s)}(\mathbf{x}) \frac{(\mathbf{x} - \mathbf{y}_n) \cdot \boldsymbol{\nu}(\mathbf{x})}{|\mathbf{x} - \mathbf{y}_n|} \frac{e^{ik_0|\mathbf{x}-\mathbf{y}_n|}}{\sqrt{|\mathbf{x}-\mathbf{y}_n|}}$$

if $(\mathbf{x} - \mathbf{y}_n) \cdot \boldsymbol{\nu}(\mathbf{x}) < 0$, where $a_n^{(s)}$ is the amplitude, and

$$(6.2) \quad u_n^{(s)}(\mathbf{x}) \approx \frac{\partial u_n^{(s)}}{\partial \nu}(\mathbf{x}) \approx 0 \quad \text{if } (\mathbf{x} - \mathbf{y}_n) \cdot \boldsymbol{\nu}(\mathbf{x}) \geq 0.$$

Since, in dimension $d = 2$,

$$\Gamma^{k_0}(\mathbf{x} - \mathbf{y}_m) \approx -\frac{e^{i\pi/4}}{2\sqrt{2\pi k_0}} \frac{e^{ik_0|\mathbf{x}-\mathbf{y}_m|}}{\sqrt{|\mathbf{x}-\mathbf{y}_m|}}$$

and

$$\frac{\partial \Gamma^{k_0}}{\partial \nu}(\mathbf{x} - \mathbf{y}_m) \approx -i \frac{\sqrt{k_0} e^{i\pi/4}}{2\sqrt{2\pi}} \frac{(\mathbf{x} - \mathbf{y}_m) \cdot \boldsymbol{\nu}(\mathbf{x})}{|\mathbf{x} - \mathbf{y}_m|} \frac{e^{ik_0|\mathbf{x} - \mathbf{y}_m|}}{\sqrt{|\mathbf{x} - \mathbf{y}_m|}},$$

then

(6.3)

$$A_{nm}[D, \omega] \approx -i \frac{\sqrt{k_0} e^{i\pi/4}}{2\sqrt{2\pi}} \int_{\partial D_{\text{illum}, \mathbf{y}_n}} a_n^{(s)}(\mathbf{x}) \left(\frac{(\mathbf{x} - \mathbf{y}_m) \cdot \boldsymbol{\nu}(\mathbf{x})}{|\mathbf{x} - \mathbf{y}_m|} + \frac{(\mathbf{x} - \mathbf{y}_n) \cdot \boldsymbol{\nu}(\mathbf{x})}{|\mathbf{x} - \mathbf{y}_n|} \right) \frac{e^{ik_0(|\mathbf{x} - \mathbf{y}_m| + |\mathbf{x} - \mathbf{y}_n|)}}{\sqrt{|\mathbf{x} - \mathbf{y}_m| |\mathbf{x} - \mathbf{y}_n|}} d\sigma(\mathbf{x}),$$

where $\partial D_{\text{illum}, \mathbf{y}_n} = \{\mathbf{x} \in \partial D : (\mathbf{x} - \mathbf{y}_n) \cdot \boldsymbol{\nu}(\mathbf{x}) < 0\}$. Equation (6.3) shows that the response matrix in this regime depends only on the boundary of the target that is illuminated. Note that if the aperture of the array is small compared to the distance from the array to the target, then the illuminated part of the target boundary $\partial D_{\text{illum}, \mathbf{y}_n}$ does not depend on \mathbf{y}_n .

6.2. Resolution analysis. In this section, our main aim is to connect the singular values and vectors of the MSR matrix to the target shape. In order to make explicit calculations we assume that the used array of transmitters and receivers is linear. A very similar analysis using the spheroidal wave functions was first done in [16].

6.2.1. The unperturbed domain. Let us consider the situation in which the array is linear and densely samples the line $\{(y, 0), y \in (-\alpha/2, \alpha/2)\}$ while the illuminated boundary ∂D_0 of the target is the line

$$\partial D_0 = \{(x, -L_F), x \in (-\beta/2, \beta/2)\}.$$

Assuming that the distance L_F from the array to the target is much larger than the diameter α of the array and the diameter β of the target, the response matrix is proportional to

$$A_{nm} = \int_{\partial D_0} e^{ik_0[|\mathbf{x} - \mathbf{y}_m| + |\mathbf{x} - \mathbf{y}_n|]} d\sigma(\mathbf{x}).$$

Using the Taylor series expansion (5.2), we find that in the Fraunhofer regime $k_0\beta^2/L_F \ll 1$, the response matrix is

$$A_{nm} = \beta e^{2ik_0L_F} e^{ik_0 \frac{y_m^2 + y_n^2}{2L_F}} \text{sinc} \left[\frac{k_0\beta}{2L_F} (y_n + y_m) \right].$$

Note that the first phase factor in the response matrix does not modify the singular values and it only modifies the singular vectors by a phase term independent of the singular value itself. In the following this factor is removed. Therefore, in the continuum approximation (writing $y_m = \alpha y/2$), the response matrix is proportional to the operator (from $L^2[-1, 1]$ to $L^2[-1, 1]$): $\mathcal{A}[D_0] = \mathcal{R}\mathcal{S}$, where \mathcal{R} is the involution operator $\mathcal{R}f(x, y) = f(-x, y)$ and \mathcal{S} is the sinc operator whose kernel is

$$\mathcal{S}(x, y) = \frac{\sin[C(x - y)]}{\pi(x - y)}, \quad x, y \in [-1, 1],$$

with $C = (k_0\beta\alpha)/(4L_F)$. The singular values $(\sigma^{(l)})_{l \geq 1}$ and singular vectors $(\psi^{(l)})_{l \geq 1}$ of the sinc operator \mathcal{S} are known and they are described in Appendix A. In particular the singular vectors are the prolate spheroidal functions which are either odd or even functions, so that $(\sigma^{(l)}, \psi^{(l)})_{l \geq 1}$ are also the singular values and vectors of \mathcal{A} . We consider the situation $C \gg 1$. According to [30], the important facts in this regime are as follows:

- (i) There are about $[2C/\pi]$ significant singular values; more exactly, the first $[2C/\pi]$ singular values are close to one, while the following ones are close to zero. The Fourier transforms of the significant singular vectors are concentrated in $(-C, C)$.
- (ii) The first singular vectors are concentrated around the center of the interval $(-1, 1)$, and they contain only low frequencies; more exactly, the singular vectors are approximately concentrated on an interval with length of the order of $1/\sqrt{C}$ centered at 0, and their Fourier transforms are approximately concentrated on an interval with length of the order of \sqrt{C} .
- (iii) The last significant singular vectors (i.e., those with indices close to $[2C/\pi]$) are concentrated at the edges of the interval $(-1, 1)$ and their Fourier transforms are approximately concentrated on $(-C, C)$.

6.2.2. The perturbed domain. Here we consider the case when the illuminated boundary ∂D of the target is the perturbed curve

$$\partial D = \{ \mathbf{x} = (x, -L_F + h(x)), x \in (-\beta/2, \beta/2) \}.$$

Denoting $\tilde{h}(y) = h(\beta y/2)$, $y \in (-1, 1)$, the response matrix in the continuum approximation is proportional to the operator

$$\mathcal{A}[D] = \mathcal{A}[D_0] - ik_0 \mathcal{RH}[D], \quad \mathcal{H}[D](x, y) = \int_{-1}^1 \tilde{h}(z) e^{iCz(x-y)} dz, \quad x, y \in (-1, 1).$$

By expanding the function $\tilde{h}(y)$ over the image basis of the unperturbed operator $\mathcal{A}[D_0]$,

$$\tilde{h}(y) = \sum_{p=1}^{\infty} \tilde{h}_p \psi^{(p)}(y), \quad y \in (-1, 1),$$

we find using (A.6) that

$$\langle \psi^{(l')}, \mathcal{H}[D] \psi^{(l)} \rangle = (\mathcal{Q}\tilde{h})_{l'l} = \left(\sum_{p=1}^{\infty} \mathcal{Q}_{l'l_p} \tilde{h}_p \right)_{l'l}$$

with

$$\mathcal{Q}_{l'l_p} = 2\pi i^{l-l'} \frac{\sqrt{\sigma^{(l)}\sigma^{(l')}}}{C} \int_{-1}^1 \psi^{(l')}(y) \psi^{(l)}(y) \psi^{(p)}(y) dy.$$

Note that $\mathcal{Q}_{l'l_p}$ is not vanishing as long as l', l, p are smaller than $[2C/\pi]$. If the response matrix corresponding to the true domain D_{true} is corrupted by an additive Gaussian white

noise, then the three imaging functionals have the following form to leading order in the perturbation (up to a multiplicative constant):

$$\mathcal{J}_j[D] = \frac{1}{2} \sum_{l=1}^{\infty} \sum_{l'=1}^{\infty} w_{j,l} w'_{j,l'} |(\mathcal{Q}\tilde{h})_{l'l} - (\mathcal{Q}\tilde{h}_{\text{true}})_{l'l} - \varepsilon_{\text{meas},l'l}|^2,$$

where $w_{1,l} = w'_{1,l} = 1$ for the first functional $j = 1$, $w_{2,l} = W(\sigma^{(l)})\mathbf{1}_{l \leq L}$ and $w'_{2,l} = 1$ for the second functional $j = 2$, and $w_{3,l} = W(\sigma^{(l)})\mathbf{1}_{l \leq L}$ and $w'_{3,l} = W'(\sigma^{(l')})\mathbf{1}_{l' \leq L'}$ for the third functional $j = 3$. Finally $\varepsilon_{\text{meas},l'l}$ are independent Gaussian random variables.

Denoting by \mathcal{W}_j the multiplication operator $(\mathcal{W}_j \hat{\varepsilon})_{l'l} = w_{j,l} w'_{j,l'} \hat{\varepsilon}_{l'l}$, the minimization problem is solved by applying the operator $(\mathcal{Q}^* \mathcal{W}_j \mathcal{Q})^{-1} \mathcal{Q}^* \mathcal{W}_j$ to the data

$$\left(\left\langle \psi^{(l')}, \frac{i}{k_0} \mathcal{R}(\mathcal{A}_{\text{meas}} - \mathcal{A}[D_0]) \psi^{(l)} \right\rangle \right)_{l',l}.$$

This gives an unbiased estimator of $(\tilde{h}_{\text{true},p})_p$.

Note that we have using (A.3) that

$$(\mathcal{Q}^* \mathcal{Q})_{p'p} = \frac{4\pi^2}{C^2} \int_{-1}^1 \int_{-1}^1 \mathcal{S}(x, y)^2 \phi^{(p')}(x) \phi^{(p)}(y) dx dy,$$

which is close to the identity operator (up to a factor $4\pi/C$) when restricted to

$$p, p' \leq [2C/\pi].$$

Therefore, we come to the following conclusions:

- (i) We can reconstruct the coefficients $\tilde{h}_{\text{true},p}$ up to $p \leq (L + L') \wedge [2C/\pi]$.
- (ii) The first coefficients \tilde{h}_p (those which are estimated with the highest accuracy) correspond to low-frequency information about the central part of the boundary ∂D .
- (iii) The coefficients \tilde{h}_p for p close to $[2C/\pi]$ correspond to high-frequency information about the edges of the boundary ∂D . This implies that if we want a sharp detection of the edges of the boundary, then we should choose a weight function that enhances the contributions of the singular vectors in the plunge region of the singular values. This was already noticed in [17].
- (iv) The coefficients $\tilde{h}_p, p = 1, \dots, [2C/\pi]$, correspond to features whose minimal wavenumber is $C/(\beta/2) = k_0 \alpha / (2L_F)$, which corresponds to a length scale of $2\lambda_0 L_F / \alpha$. This is the classical Rayleigh resolution formula.

7. Construction of an initial guess. In this section we develop a weighted subspace migration imaging functional for constructing a good initial guess. The idea behind this is to use the asymptotic formulation of the response matrix obtained in the previous sections. We will show the optimality in the presence of an additive noise of the proposed method for choosing the prior guess. Optimality is to be understood in the sense that the location of the maximum of the proposed imaging functional is exactly the maximum likelihood estimator of a sampling of the inclusion shape.

7.1. Measurements at a single frequency. We first construct an initial guess from measurements of the response matrix at a single frequency ω . Let us introduce the vector field

$$(7.1) \quad \mathbf{g}(\mathbf{x}, \omega) = \left(\frac{\exp(ik_0|\mathbf{x} - \mathbf{y}_n|)}{\sqrt{N}} \right)_{n=1, \dots, N}.$$

A good initial guess would be obtained using a weighted subspace migration [17]:

$$(7.2) \quad \begin{aligned} \mathcal{I}_{\text{SM}}(\mathbf{x}, \omega, \mathbf{w}) &= \overline{\mathbf{g}(\mathbf{x}, \omega)}^T \sum_{l=1}^N w_l(\mathbf{x}, \omega) \mathbf{v}_{\text{meas}}^{(l)}[\omega] \mathbf{v}_{\text{meas}}^{(l)}[\omega]^T \overline{\mathbf{g}(\mathbf{x}, \omega)} \\ &= \sum_{l=1}^N w_l(\mathbf{x}, \omega) \langle \mathbf{g}(\mathbf{x}, \omega), \mathbf{v}_{\text{meas}}^{(l)}[\omega] \rangle^2, \end{aligned}$$

where $(\mathbf{v}_{\text{meas}}^{(l)}[\omega])_{l=1, \dots, N}$ are the singular vectors of $\mathbf{A}_{\text{meas}}[\omega]$ and $\mathbf{w}(\mathbf{x}, \omega) = (w_l(\mathbf{x}, \omega))_{l=1, \dots, N}$ are filter (complex) weights.

Consider in particular the weights

$$w_l^{(1)}(\mathbf{x}, \omega) = \sigma_{\text{meas}}^{(l)}[\omega], \quad w_l^{(2)}(\mathbf{x}, \omega) = \exp\left(-i2 \arg \langle \mathbf{g}(\mathbf{x}, \omega), \mathbf{v}_{\text{meas}}^{(l)}[\omega] \rangle\right) \mathbf{1}_{l \leq L},$$

where L is the number of the nonzero singular values (i.e., the dimension of the image space of $\mathbf{A}_{\text{meas}}[\omega]$). Then $\mathcal{I}_{\text{SM}}(\mathbf{x}, \omega, \mathbf{w}^{(1)})$ corresponds to the Kirchhoff migration:

$$(7.3) \quad \mathcal{I}_{\text{SM}}(\mathbf{x}, \omega, \mathbf{w}^{(1)}) = \mathcal{I}_{\text{KM}}(\mathbf{x}, \omega) := \overline{\mathbf{g}(\mathbf{x}, \omega)}^T \mathbf{A}_{\text{meas}}[\omega] \overline{\mathbf{g}(\mathbf{x}, \omega)}.$$

Moreover, we have the following connection of $\mathcal{I}_{\text{SM}}(\mathbf{x}, \omega, \mathbf{w}^{(2)})$ to the MUSIC (multiple signal classification) algorithm:

$$(7.4) \quad \begin{aligned} \mathcal{I}_{\text{MUSIC}}(\mathbf{x}, \omega) &= \left\| \mathbf{g}(\mathbf{x}, \omega) - \sum_{l=1}^L \langle \mathbf{v}_{\text{meas}}^{(l)}[\omega], \mathbf{g}(\mathbf{x}, \omega) \rangle \mathbf{v}_{\text{meas}}^{(l)}[\omega] \right\|^{-1/2} \\ &= \left(1 - \sum_{l=1}^L |\langle \mathbf{v}_{\text{meas}}^{(l)}[\omega], \mathbf{g}(\mathbf{x}, \omega) \rangle|^2 \right)^{-1/2} \\ &= (1 - \mathcal{I}_{\text{SM}}(\mathbf{x}, \omega, \mathbf{w}^{(2)}))^{-1/2}. \end{aligned}$$

The next subsection will make it clear that an appropriate weighted subspace migration is optimal to find an initial guess in the presence of additive noise.

7.2. Optimality. We present here a particular context in which a weighted subspace migration imaging functional gives the “optimal” approach to choosing the prior guess for the scatterer support D , or rather the illuminated part of its boundary. This generalizes the results of [7] obtained for a point target to the case of an extended target.

For simplicity, we drop in this section the dependence on the frequency ω from the notation. We assume the following model for the data:

$$\mathbf{A}_{\text{meas}} \sim \sum_{l=1}^L \tau_l \mathbf{g}(\mathbf{x}_l) \mathbf{g}(\mathbf{x}_l)^T + \sigma \mathbf{N}.$$

Here L is an estimated signal space dimension, $\mathbf{N} \in \mathbb{R}^{N \times N}$ has zero-mean jointly circularly symmetric Gaussian distributed entries and models additive noise, $\mathbf{g}(\mathbf{x})$ is defined by (7.1), and $\mathbf{g}(\mathbf{x}_j) \perp \mathbf{g}(\mathbf{x}_l), j \neq l$, i.e., $\langle \mathbf{g}(\mathbf{x}_j), \mathbf{g}(\mathbf{x}_l) \rangle = 0$. Recall that the measured response matrix is symmetrized by the straightforward formula $\mathbf{A} \rightarrow (\mathbf{A} + \mathbf{A}^T)/2$, so the additive noise also undergoes the same transformation. It is also worth emphasizing that the orthogonality assumption $\mathbf{g}(\mathbf{x}_j) \perp \mathbf{g}(\mathbf{x}_l), j \neq l$, is ideal. In fact, if the sampling points \mathbf{x}_j are well separated, the distance between the array and the target is large, and the illumination is uniform in the angle space, then this orthogonality assumption holds approximately and can be used to provide a good initial guess.

Given the observations \mathbf{A}_{meas} , we find by using the Bayes theorem with the Jeffreys prior for the parameters (a noninformative prior distribution) that the likelihood function of the parameters $\mathbf{X} = (\mathbf{x}_j)_{j=1, \dots, L}$, $\boldsymbol{\tau} = (\tau_1, \dots, \tau_L)$, and σ^2 is proportional to

$$(7.5) \quad l_0(\mathbf{X}, \boldsymbol{\tau}, \sigma^2 \mid \mathbf{A}_{\text{meas}}) = \frac{1}{\sigma^{L^2+L+1}} \exp\left(-\frac{\|\mathbf{A}_{\text{meas}} - \sum_{l=1}^L \tau_l \mathbf{g}(\mathbf{x}_l) \mathbf{g}(\mathbf{x}_l)^T\|_F^2}{2\sigma^2}\right)$$

with the subscript F representing the Frobenius norm. The maximum likelihood estimate of \mathbf{X} and the nuisance parameters σ and $\boldsymbol{\tau}$ are found by maximizing the likelihood function (7.5) with respect to these:

$$(\hat{\mathbf{X}}, \hat{\boldsymbol{\tau}}, \hat{\sigma}^2) = \underset{\mathbf{X}, \boldsymbol{\tau}, \sigma^2 \mid \mathbf{g}(\mathbf{x}_j) \perp \mathbf{g}(\mathbf{x}_l), j \neq l}{\text{argmax}} \quad l_0(\mathbf{X}, \boldsymbol{\tau}, \sigma^2 \mid \mathbf{A}_{\text{meas}}).$$

We first eliminate σ^2 by requiring

$$\frac{\partial l_0(\mathbf{X}, \boldsymbol{\tau}, \sigma^2 \mid \mathbf{A}_{\text{meas}})}{\partial \sigma} = 0.$$

This gives

$$\hat{\sigma}^2 = \frac{\|\mathbf{A}_{\text{meas}} - \sum_{l=1}^L \tau_l \mathbf{g}(\mathbf{x}_l) \mathbf{g}(\mathbf{x}_l)^T\|_F^2}{L^2 + L + 1},$$

and the likelihood ratio is proportional to

$$l_0(\mathbf{X}, \boldsymbol{\tau}, \hat{\sigma}^2 \mid \mathbf{A}_{\text{meas}}) \simeq \left\| \mathbf{A}_{\text{meas}} - \sum_{l=1}^L \tau_l \mathbf{g}(\mathbf{x}_l) \mathbf{g}(\mathbf{x}_l)^T \right\|_F^{-(L^2+L+1)/2}.$$

Note that we have

$$\left\| \mathbf{A}_{\text{meas}} - \sum_{l=1}^L \tau_l \mathbf{g}(\mathbf{x}_l) \mathbf{g}(\mathbf{x}_l)^T \right\|_F^2 = \left\| \tilde{\mathbf{v}} - \sum_{l=1}^L \tau_l \tilde{\mathbf{g}}(\mathbf{x}_l) \right\|_2^2$$

for $\tilde{\mathbf{v}} = \sum_{l=1}^N \sigma_{\text{meas}}^{(l)} \mathbf{v}_{\text{meas}}^{(l)} \otimes \mathbf{v}_{\text{meas}}^{(l)}$ and $\tilde{\mathbf{g}}(\mathbf{x}_l) = \mathbf{g}(\mathbf{x}_l) \otimes \mathbf{g}(\mathbf{x}_l)$. Using that $\tilde{\mathbf{g}}(\mathbf{x}_j) \perp \tilde{\mathbf{g}}(\mathbf{x}_l)$ for $j \neq l$ we find

$$\left\| \mathbf{A}_{\text{meas}} - \sum_{l=1}^L \tau_l \mathbf{g}(\mathbf{x}_l) \mathbf{g}(\mathbf{x}_l)^T \right\|_F^2 = \sum_{l=1}^L \|\tilde{\mathbf{v}} - \tau_l \tilde{\mathbf{g}}(\mathbf{x}_l)\|_2^2 - (L-1) \|\tilde{\mathbf{v}}\|_2^2.$$

On the other hand, note that

$$\hat{\tau} = \underset{\tau}{\operatorname{argmin}} \sum_{l=1}^L \|\tilde{\mathbf{v}} - \tau_l \tilde{\mathbf{g}}(\mathbf{x}_l)\|_2^2 = \langle \tilde{\mathbf{v}}, \tilde{\mathbf{g}}(\mathbf{x}_l) \rangle_{l=1, \dots, L},$$

where we have taken into account the fact that $\|\tilde{\mathbf{g}}(\mathbf{x}_l)\|_2 = 1$. We therefore conclude that the estimate $\hat{\mathbf{X}}$ derives from

$$\hat{\mathbf{X}} = \underset{\mathbf{X} | \mathbf{g}(\mathbf{x}_j) \perp \mathbf{g}(\mathbf{x}_i), j \neq i}{\operatorname{argmin}} \sum_{l=1}^L \|\tilde{\mathbf{v}} - \langle \tilde{\mathbf{v}}, \tilde{\mathbf{g}}(\mathbf{x}_l) \rangle \tilde{\mathbf{g}}(\mathbf{x}_l)\|_2^2.$$

Note that

$$\begin{aligned} \sum_{l=1}^L \|\tilde{\mathbf{v}} - \langle \tilde{\mathbf{v}}, \tilde{\mathbf{g}}(\mathbf{x}_l) \rangle \tilde{\mathbf{g}}(\mathbf{x}_l)\|_2^2 &= L \|\tilde{\mathbf{v}}\|_2^2 - \sum_{l=1}^L |\langle \tilde{\mathbf{g}}(\mathbf{x}_l), \tilde{\mathbf{v}} \rangle|^2 \\ &= L \|\tilde{\mathbf{v}}\|_2^2 - \sum_{l=1}^L \left| \sum_{l'=1}^N \sigma_{\text{meas}}^{(l')} \langle \mathbf{g}(\mathbf{x}_l, \omega), \mathbf{v}_{\text{meas}}^{(l')} \rangle \right|^2. \end{aligned}$$

From this representation we find that the estimates of the locations $\mathbf{X} = (\mathbf{x}_l)_{l=1, \dots, L}$ can be expressed in terms of the weighted subspace migration \mathcal{I}_{SM} with the weights $\mathbf{w}^{(1)} = (\sigma_{\text{meas}}^{(l)})_{l=1, \dots, L}$, which is the KM functional \mathcal{I}_{KM} by (7.3):

$$(7.6) \quad \hat{\mathbf{X}} = \underset{\mathbf{X} | \mathbf{g}(\mathbf{x}_j) \perp \mathbf{g}(\mathbf{x}_i), j \neq i}{\operatorname{argmax}} \sum_{l=1}^L |\mathcal{I}_{\text{KM}}(\mathbf{x}_l, \omega)|^2.$$

This then gives an algorithm for the prior guess:

- (i) Compute the KM map $\mathcal{I}_{\text{KM}}(\mathbf{x}, \omega)$.
- (ii) By parameterizing the curve corresponding to the illuminated part of the boundary of the inclusion with L points separated by approximately $\lambda_0/2$, and by maximizing $\sum_{l=1}^L |\mathcal{I}_{\text{KM}}(\mathbf{x}_l, \omega)|^2$ over the positions of the L points, we obtain the initial guess. Here, λ_0 is the central wavelength.

Note that the weighted subspace migration with the weights $\mathbf{w}^{(1)}$, corresponding to KM, is more appropriate for the initial guess than the weighted subspace migration \mathcal{I}_{SM} with the weights $\mathbf{w}^{(2)}$, corresponding to MUSIC.

We remark that the implementation regarding the identification of the points approximating the boundary may be carried out recursively. It is then relevant to project the signal space and illumination vectors on the complement of the range of the illumination space associated with the points already identified. That is, one may implement the prior guess identification as follows:

- (i') Identify $\hat{\mathbf{x}}_1$ as the spatial location maximizing the imaging function $|\mathcal{I}_{\text{KM}}(\mathbf{x}, \omega)|^2$.
- (ii') Given $\hat{\mathbf{x}}_1, \dots, \hat{\mathbf{x}}_{k-1}$ identify $\hat{\mathbf{x}}_k$ as the location separated approximately by $\lambda_0/2$ from previously identified points and maximizing the imaging function associated with the projected signal space and illumination vectors:

$$\check{\mathbf{A}}_{\text{meas}} = \mathbf{\Pi}_{1,k-1} \mathbf{A}_{\text{meas}} \mathbf{\Pi}_{1,k-1}, \quad \check{\mathbf{g}}(\mathbf{x}_k) = \mathbf{\Pi}_{1,k-1} \mathbf{g}(\mathbf{x}_k)$$

for $\mathbf{\Pi}_{1,k-1} \equiv \mathbf{I} - \sum_{j=1}^{k-1} \mathbf{g}(\hat{\mathbf{x}}_j) \mathbf{g}(\hat{\mathbf{x}}_j)^T$.

7.3. Measurements at multiple frequencies. In the case of measurements at multiple frequencies one can use the imaging functional

$$(7.7) \quad \mathcal{I}_{\text{SM}}(\mathbf{x}, \mathbf{w}) = \frac{1}{P} \sum_{p=1}^P \mathcal{I}_{\text{SM}}(\mathbf{x}, \omega_p, \mathbf{w}),$$

where $\mathcal{I}_{\text{SM}}(\mathbf{x}, \omega_p, \mathbf{w})$ is given by (7.2) and P is the number of used frequencies, in order to get an initial guess of the illuminated part of the inclusion D . This proposition comes from the following approximate calculations. For any smooth function $\tilde{a}(\mathbf{y})$ and boundary ∂D ,

$$\begin{aligned} & \sum_{m,n=1}^N \frac{1}{P} \sum_{p=1}^P e^{-i\omega_p(|\mathbf{x}-\mathbf{y}_m|+|\mathbf{x}-\mathbf{y}_n|)} \int_{\partial D} \tilde{a}(\mathbf{y}) e^{i\omega_p(|\mathbf{y}-\mathbf{y}_m|+|\mathbf{y}-\mathbf{y}_n|)} d\sigma(\mathbf{y}) \\ &= \sum_{m,n=1}^N \int_{\partial D} \tilde{a}(\mathbf{y}) \left[\frac{1}{P} \sum_{p=1}^P e^{-i\omega_p(|\mathbf{x}-\mathbf{y}_m|-|\mathbf{y}-\mathbf{y}_m|+|\mathbf{x}-\mathbf{y}_n|-|\mathbf{y}-\mathbf{y}_n|)} \right] d\sigma(\mathbf{y}) \\ &\approx \sum_{m,n=1}^N \int_{\partial D} \tilde{a}(\mathbf{y}) \delta(|\mathbf{x}-\mathbf{y}_m|+|\mathbf{x}-\mathbf{y}_n|-|\mathbf{y}-\mathbf{y}_m|-|\mathbf{y}-\mathbf{y}_n|) d\sigma(\mathbf{y}) \\ &\approx N^2 \int_{\partial D} \tilde{a}(\mathbf{y}) \delta(\mathbf{y}-\mathbf{x}) d\sigma(\mathbf{y}) \approx \begin{cases} N^2 \tilde{a}(\mathbf{x}) & \text{if } \mathbf{x} \in \partial D, \\ 0 & \text{elsewhere.} \end{cases} \end{aligned}$$

It is possible to do a detailed analysis of the previous sum along the same lines as in [20]. It would exhibit that the final Dirac distribution is in fact a sharp peak whose width depends on the bandwidth and on the geometry of the array. Here this approximate calculation is sufficient to justify that (7.7) is a reasonable initial guess. Therefore, it follows from (6.3) that in order to construct an initial guess in the case of both permittivity and permeability contrasts one can use (7.7). This is good in absence of additive noise. In the presence of additive Gaussian white noise (which gives independent noises for each frequency), we can repeat the Bayesian arguments of the previous subsection, and we find the following algorithm for the prior guess:

- (i) Compute the KM map $\mathcal{I}_{\text{KM}}(\mathbf{x}, \omega)$.
- (ii) By parameterizing the curve corresponding to the illuminated part of the boundary of the inclusion with L points separated by approximately $\lambda_0/2$, and by maximizing $\sum_{p=1}^P \sum_{l=1}^L |\mathcal{I}_{\text{KM}}(\mathbf{x}_l, \omega_p)|^2$ over the positions of the L points, we obtain the initial guess. Here, λ_0 is the central wavelength.

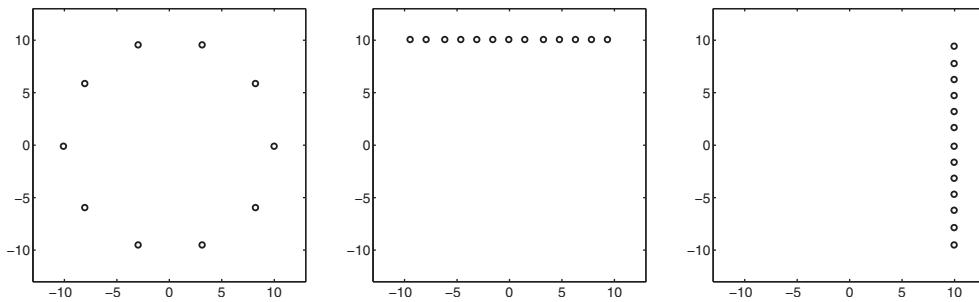


Figure 1. From left to right: configuration (8.1) (full aperture) and configurations (8.2) and (8.3) (limited-aperture).

Note that we should look for the maximum of the sum of the square moduli of the KM functionals in order to exploit the multifrequency information optimally. The fact that the relevant operation is the sum of the squares comes from the fact that the additive noise matrices are assumed to be independent for different frequencies.

8. Numerical illustrations. In this section, we illustrate our algorithms for recovering the shape of a domain from multistatic response measurements. The direct solver is implemented based on the boundary integral representation of the solution to the corresponding transmission problem. Throughout this section, we assume that the permeability and permittivity contrasts are known. We set $\mu_0 = 1$, $\mu = 5$, $\epsilon_0 = 1$, and $\epsilon = 2$. The coincident transmitter and receiver arrays $\{\mathbf{y}_1, \dots, \mathbf{y}_N\}$ are located at either one of the following positions:

$$(8.1) \quad \mathbf{y}_j = 10(\cos((j - 1)\pi/5), \sin((j - 1)\pi/5)), \quad j = 1, \dots, 10,$$

$$(8.2) \quad \mathbf{y}_j = ((-3.5 + 0.5j)\pi, 10), \quad j = 1, \dots, 13,$$

$$(8.3) \quad \mathbf{y}_j = (10, (-3.5 + 0.5j)\pi), \quad j = 1, \dots, 13.$$

Configuration (8.1) corresponds to a full aperture, while (8.2) and (8.3) correspond to limited-view configurations; see Figure 1.

We suppose that D is illuminated by a time-harmonic point source acting at \mathbf{y}_j with frequency ω . Note that the corresponding wavenumber is $k_0 = \omega$.

We first use the Kirchhoff migration functional (7.3) with frequency $\omega = 2$ to get an initial guess. We divide the search domain into 30×30 subrectangles and compute $\mathcal{I}_{\text{KM}}(\mathbf{x}_l, \omega)$ at each nodal point \mathbf{x}_l in the search domain. We get the set of illuminated points such that

$$|\mathcal{I}_{\text{KM}}(\mathbf{x}, \omega)| > 0.9 \times \max |\mathcal{I}_{\text{KM}}|.$$

Taking the average of the illuminated points, we obtain a center point. To find a disk-shaped initial guess, we test for a couple of radii, which are 0.5, 1, and 1.5 times the distance from the obtained center to one of the illuminated points, which among these three circles passes through the largest number of illuminated points. Figure 2 shows that the disk-shaped initial guess is close to the true inclusion. Moreover, it depends on the configuration of the transmitters and receivers array.

Now, we turn to the optimization procedures. We first compute the SVD of the MSR matrix. Figure 3 shows that the number of significant singular vectors is less than 10.

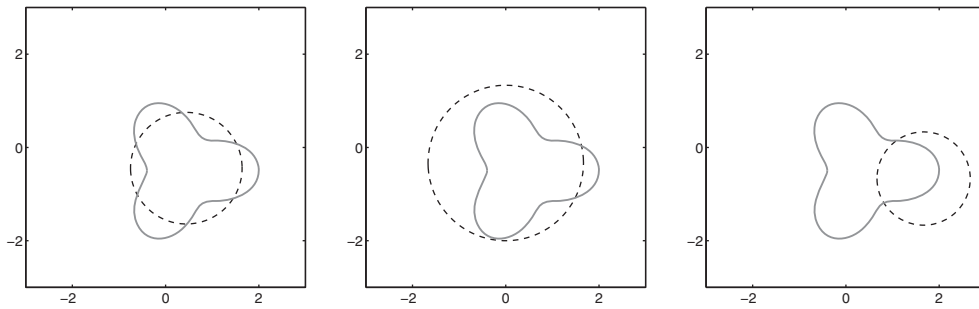


Figure 2. Kirchhoff migration for getting initial guesses. The first is from the measurement (8.1), and the second and the third are from (8.2) and (8.3), respectively.

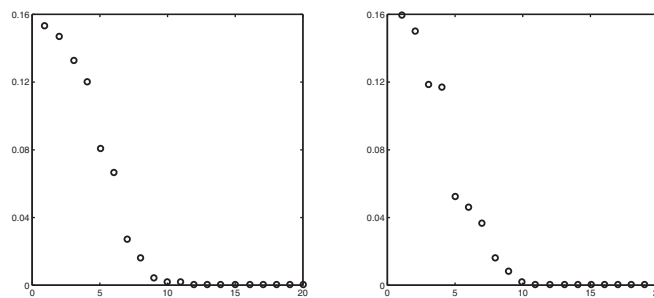


Figure 3. Singular values of the MSR matrix with 20 transmitters and 20 receivers. The number of significant singular values is less than 10 out of 20. The figure on the left corresponds to the inclusion which is the unit disk centered at the origin and the one on the right corresponds to a general shaped inclusion.

We now choose the weights. The first weights $W(\sigma_{\text{meas}}^{(l)})$ are taken at the first, second, and third iteration as follows:

- $W(\sigma_{\text{meas}}^{(l)}) = 1$ for $1 \leq l \leq 5$ and 0 elsewhere,
- $W(\sigma_{\text{meas}}^{(l)}) = 1$ for $6 \leq l \leq 10$ and 0 elsewhere,
- $W(\sigma_{\text{meas}}^{(l)}) = 1$ for $1 \leq l \leq 10$ and 0 elsewhere.

While at the first step the low-frequency oscillations of the boundary are recovered, in the second step the high-frequency part is reconstructed. In the third iteration, we use all the singular vectors of the MSR matrix. We choose the number of iterations equal to six or nine. We can of course put the stopping criterion based on the measurement difference between the computed and the measured data. The pattern of choosing weights is repeated for each three steps. Moreover, the second (dual) weights $W'(\sigma^{(l)}[D_j])$ are chosen to be the same as $W(\sigma_{\text{meas}}^{(l)})$. Note that since increasing the number of the transmitters and the receivers does not change the number of significant singular values, we can use the weights defined above even with denser arrays. Note also that in the presence of a high level of noise, we should choose fewer singular vectors than in the noiseless case. But we could use the same pattern of choosing weights as here.

Now, consider an extended target which is a perturbation of the disk D_0 with unit radius $r_0 = 1$. We test the proposed shape reconstruction schemes. On the one hand, in the left

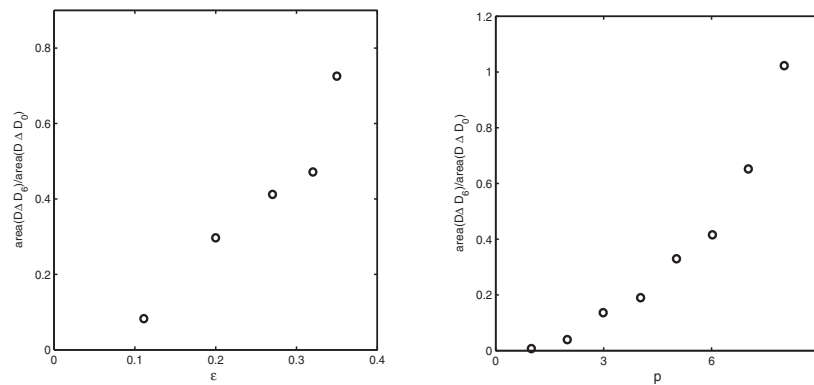


Figure 4. The difference between initial and reconstructed shapes depends on the magnitude of perturbations ε , the radius of the target $r_0 = 1$, and the number p of oscillations of the perturbation. If ε is relatively small and $p < 2k_0r_0$, then method 1 works well. D_6 is the reconstructed target after six iterations.

picture of Figure 4, we fix the frequency $\omega = 1$ and investigate the performance of method 1 as a function of ε for $\partial D = \partial D_0 + h\nu$ and $h = \varepsilon(1 + 2\cos(3\theta))$. On the other hand, in the right picture of Figure 4, fixing $\omega = 1$ and $\varepsilon = 0.1$, we also test the validity of method 1 as a function of the number of oscillations p of the perturbation $h = 0.1(1 + 2\cos(p\theta))$. It turns out that if $p < 2k_0r_0$, then the numerical scheme works well, as predicted by the resolution theory of section 5.2. In Figure 4, $|D\Delta D_0|$ and $|D\Delta D_6|$ are respectively the symmetric differences between D and D_0 and D and D_6 .

8.1. Reconstruction examples. In the following two examples, we consider the influence on the reconstruction of the frequency and an additive noise in the MSR measurements.

Example 1. In this example, $h = 0.2(1 + 2\cos(p\theta))$, $p = 3$ and 6 , and the transmitter and receiver arrays are given by (8.1). The chosen operating frequencies are $\omega = 1$ and $\omega = 2$. In Figure 5, $p = 6$ and $\omega = 2$. The initial guess was constructed using (7.3). We start with the initial guess shown as a dashed line and show the shape D_6 obtained after six iterations with a dark solid line. As shown in Figure 5, in the case of noise, method 3 improves the shape relatively more slow than methods 1 and 2. In Figure 6, we use $p = 3$ and $\omega = 1$. While method 1 does not improve the shape relative to the initial guess, methods 2 and 3 do. Moreover, method 3 has the best resolution.

Example 2. Here $\omega = 1$ and $p = 3$. In Figure 7, the first row is the reconstruction D_6 without error, while the second and third rows are with 5% and 10% relative L^2 -error in MSR matrix, respectively. Comparing to Figure 5, method 1 better detects the shape because D is less oscillatory. Method 1 is more stable than methods 2 and 3.

Example 3. The example in Figure 8 is the reconstruction of kite-shaped D with 0% and 10% noise. Methods 1 regularizes the image, while methods 2 and 3 catch better details.

Example 4. The examples in Figure 9 show how the reconstructed images depend on the location of transmitter and receiver arrays in the limited-view case. When the arrays coincide, the part in front of the array is better reconstructed.

Example 5. The example in Figure 10 reveals the limitation of the shape reconstruction of highly nonconvex or thin shapes. Here we used measurement configuration (8.1).

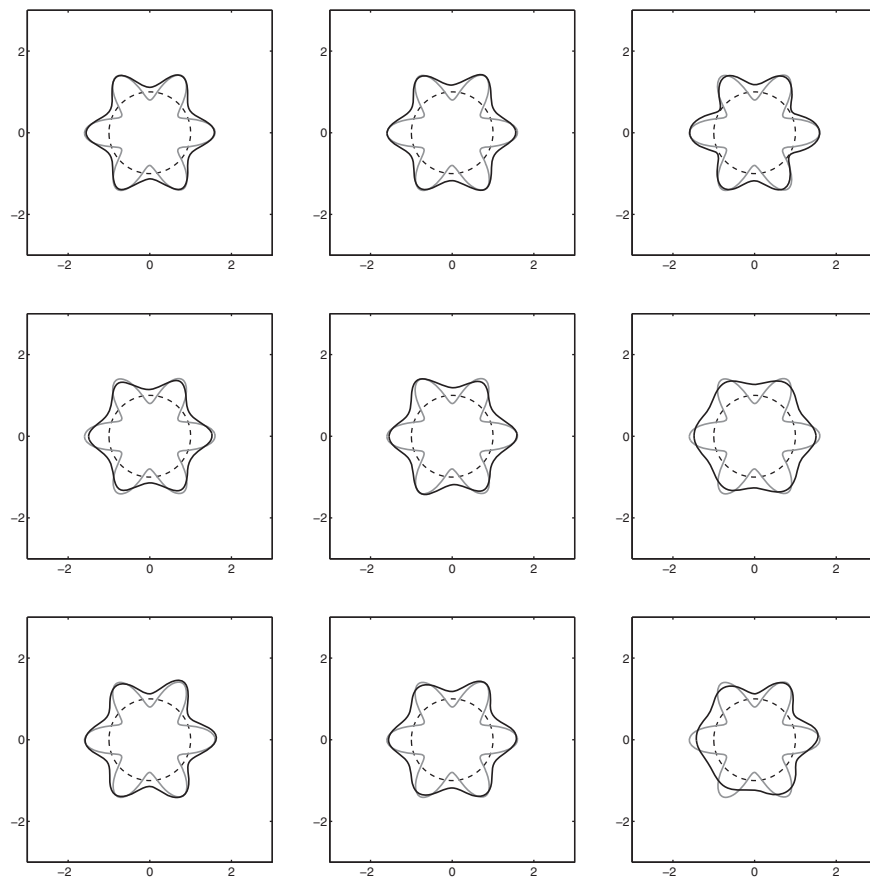


Figure 5. The first, second, and third columns are from methods 1, 2, and 3, respectively, obtained with $\omega = 2$ in the case of a full aperture array. The first row is the reconstruction without error and the second and third rows are with 5% and 10% relative L^2 -error in MSR matrix, respectively.

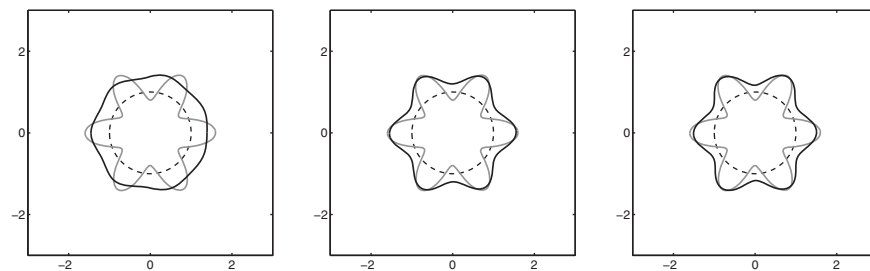


Figure 6. The first, second, and third figures are respectively from methods 1, 2, and 3 in the noiseless case. They are obtained with $\omega = 1$. Methods 2 and 3 can detect (highly compared to the wavelength) oscillatory boundary perturbations which are undetectable with method 1.

9. The elastic case. In this section we extend the results and methods introduced for the Helmholtz equation to linear elasticity. Multistatic imaging of small elastic inclusions was developed in [4, 8, 11]. Here we consider extended targets of size larger than the shear

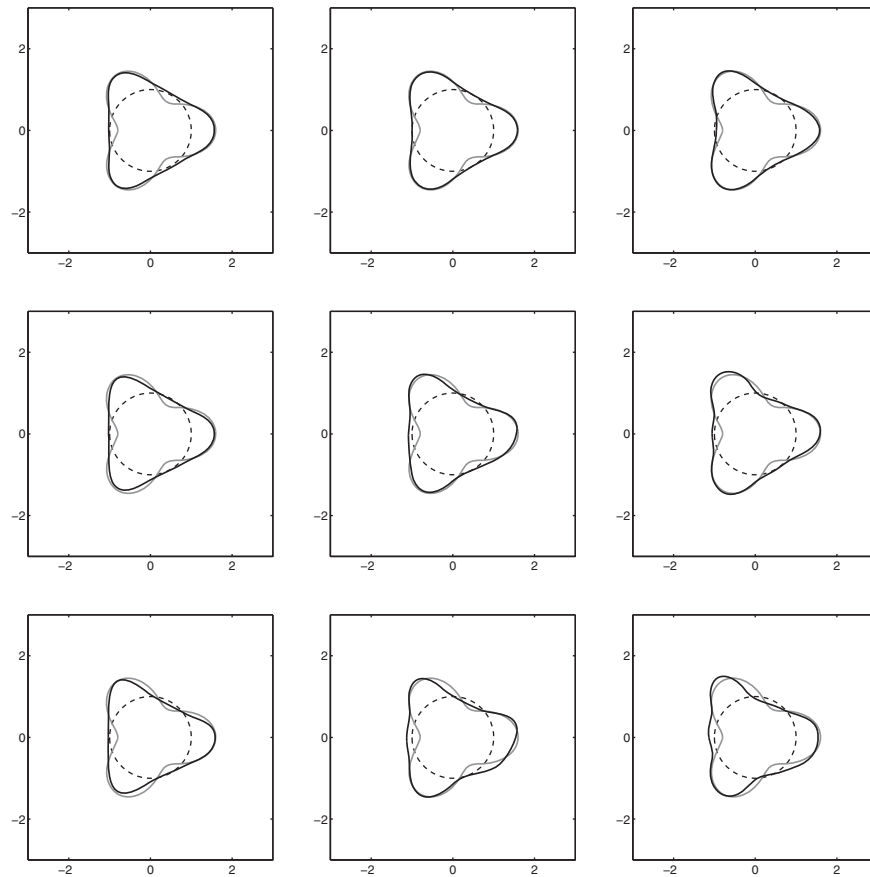


Figure 7. The first row is the reconstruction without error, and the second and third rows are with 5% and 10% relative L^2 -error in MSR matrix, respectively. Columns are reconstructions by methods 1, 2, and 3, respectively. Method 1 is more stable than methods 2 and 3.

and compressional wavelengths and propose original optimal control algorithms for shape reconstruction from MSR measurements at multiple frequencies. Again, we give natural shape representations in terms of backpropagation of significant singular vectors of MSR matrices. Compared to the scalar case, the main difficulties come from the vectorial aspect of the elasticity equations and, in particular, the coupling between the shear and compressional waves. As a consequence, deriving an initial guess based on a high-frequency asymptotic approach is a nontrivial task. Moreover, the explicit calculations of the shape derivatives of the proposed optimal control algorithms are quite involved. In connection with our results, it is worth referring to the recent work [15], where an adjoint-based formulation for reconstructing an elastic target was presented.

9.1. Problem formulation. Let the constants (λ, μ) denote the background Lamé coefficients that are the elastic parameters in the absence of any elastic inclusion. Let $\mathcal{L}_{\lambda, \mu}$ denote the Lamé operator

$$\mathcal{L}_{\lambda, \mu} \mathbf{u} = (\lambda + \mu) \nabla (\nabla \cdot \mathbf{u}) + \mu \Delta \mathbf{u}.$$

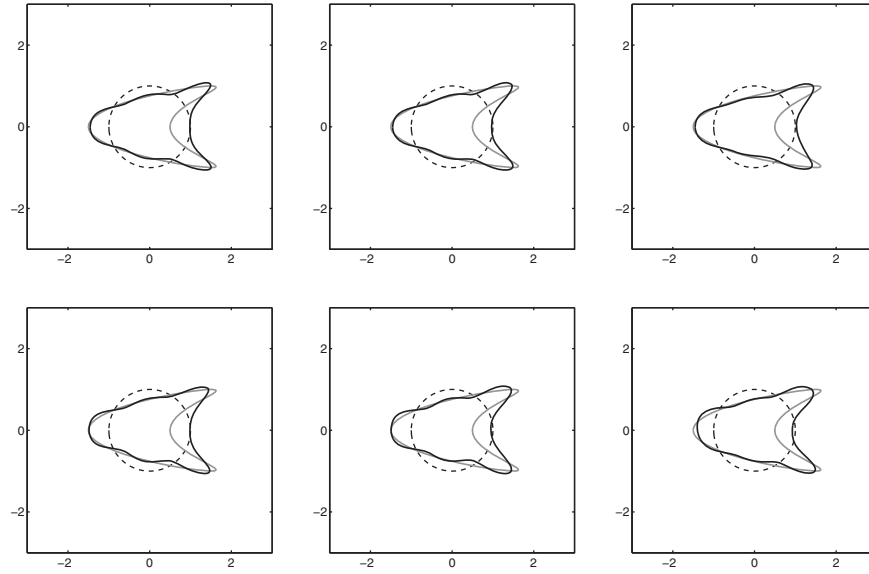


Figure 8. The first row is the reconstruction of a kite-shaped target by methods 1, 2, and 3 without error, and the second row is with 10% relative L^2 -error in MSR matrix.

Let ρ be the density of the background medium. Let $\mathbf{G}^\omega(\mathbf{x}, \mathbf{y})$ be the outgoing Green function for $\mathcal{L}_{\lambda,\mu} + \omega^2 \rho$ in \mathbb{R}^2 corresponding to a Dirac mass at \mathbf{y} . That is, \mathbf{G}^ω is the solution to

$$\mathcal{L}_{\lambda,\mu} \mathbf{G}^\omega(\mathbf{x}, \mathbf{y}) + \omega^2 \rho \mathbf{G}^\omega(\mathbf{x}, \mathbf{y}) = -\delta_{\mathbf{y}}(\mathbf{x}) \mathbf{I} \quad \text{in } \mathbb{R}^2,$$

subject to the outgoing radiation conditions. Here \mathbf{I} is the 2×2 identity matrix. We recall the reciprocity relation: $\mathbf{G}^\omega(\mathbf{y}, \mathbf{x}) = \mathbf{G}^\omega(\mathbf{x}, \mathbf{y})^T$. Denote

$$c_p = \sqrt{\frac{\lambda + 2\mu}{\rho}}, \quad c_s = \sqrt{\frac{\mu}{\rho}}.$$

The Green function is given by

$$G_{jl}^\omega(\mathbf{x}, \mathbf{y}) = \frac{i}{4\mu} \delta_{jl} H_0^{(1)} \left(\frac{\omega |\mathbf{x} - \mathbf{y}|}{c_s} \right) + \frac{i}{4\omega^2 \rho} \partial_j \partial_l \left(H_0^{(1)} \left(\frac{\omega |\mathbf{x} - \mathbf{y}|}{c_s} \right) - H_0^{(1)} \left(\frac{\omega |\mathbf{x} - \mathbf{y}|}{c_p} \right) \right), \quad j, l = 1, 2.$$

Suppose that the soft elastic inclusion D has the pair of Lamé constants $(\tilde{\lambda}, \tilde{\mu})$ and the density $\tilde{\rho}$. Let $\mathcal{L}_{\lambda,\mu}$ and $\mathcal{L}_{\tilde{\lambda},\tilde{\mu}}$ be the Lamé systems corresponding to the Lamé parameters (λ, μ) and $(\tilde{\lambda}, \tilde{\mu})$, respectively. We will denote by $\tilde{\mathbf{G}}^\omega(\mathbf{x}, \mathbf{y})$ the outgoing Green function associated with $(\tilde{\lambda}, \tilde{\mu}, \tilde{\rho})$. We assume that D is illuminated by a time-harmonic point source acting at the point \mathbf{y} in the direction $\boldsymbol{\gamma}$ with frequency ω . The displacement field $\mathbf{u}(\cdot, \mathbf{y}, \boldsymbol{\gamma})$ is given as

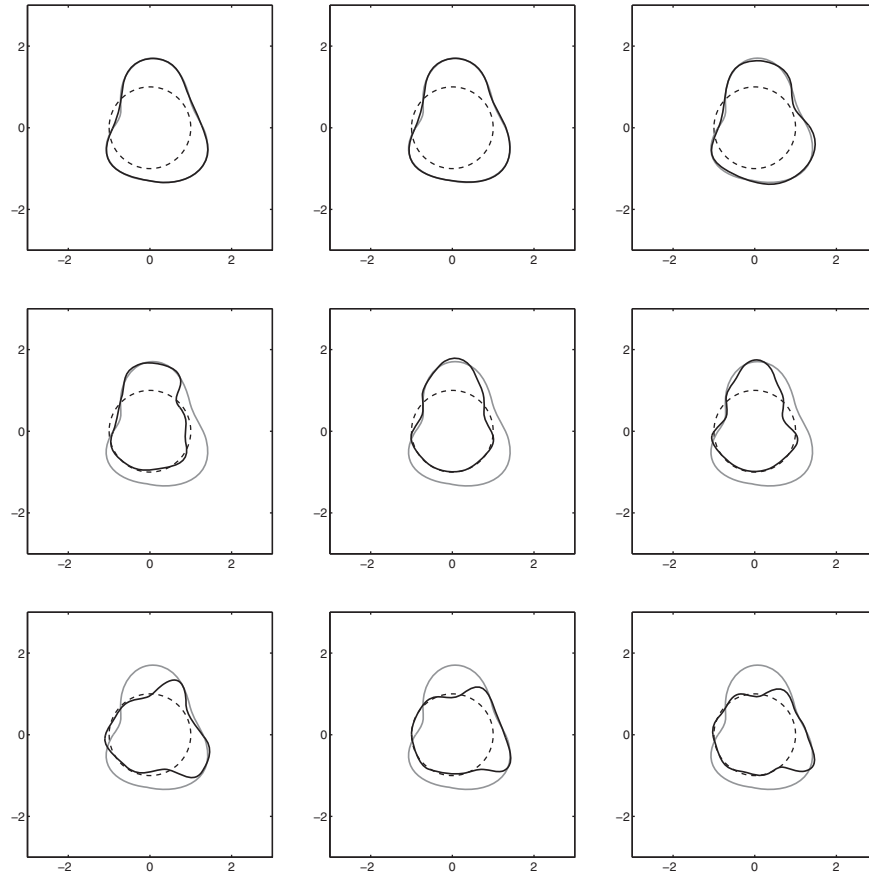


Figure 9. Method 2 with different source-receiver points. The first, second, and third images correspond to (8.1), (8.2), and (8.3), respectively.

the solution to the transmission problem:

$$(9.1) \quad \begin{cases} \mathcal{L}_{\lambda,\mu} \mathbf{u} + \omega^2 \rho \mathbf{u} = -\gamma \delta_{\mathbf{y}} & \text{in } \mathbb{R}^2 \setminus \overline{D}, \\ \mathcal{L}_{\tilde{\lambda},\tilde{\mu}} \mathbf{u} + \omega^2 \tilde{\rho} \mathbf{u} = 0 & \text{in } D, \\ \mathbf{u}|_+ - \mathbf{u}|_- = 0 & \text{on } \partial D, \\ \frac{\partial \mathbf{u}}{\partial n}|_+ - \frac{\partial \mathbf{u}}{\partial \tilde{n}}|_- = 0 & \text{on } \partial D, \\ \mathbf{u} \text{ satisfies the outgoing radiation conditions.} \end{cases}$$

Here $\partial/\partial n$ and $\partial/\partial \tilde{n}$ denote the conormal derivatives associated with $\mathcal{L}_{\lambda,\mu}$ and $\mathcal{L}_{\tilde{\lambda},\tilde{\mu}}$.

Suppose that we have two coincident transmitter and receiver arrays $\{\mathbf{y}_1, \dots, \mathbf{y}_N\}$ of N elements, used to detect the inclusion. Let $\{\gamma_1^i, \dots, \gamma_N^i\}$ and $\{\gamma_1^o, \dots, \gamma_N^o\}$ be the corresponding unit directions of incident fields/observation directions. The MSR matrix describes the transmit-receive process performed from this array. In the presence of the inclusion the displacement field induced on the n th receiving element from the scattering of an incident wave

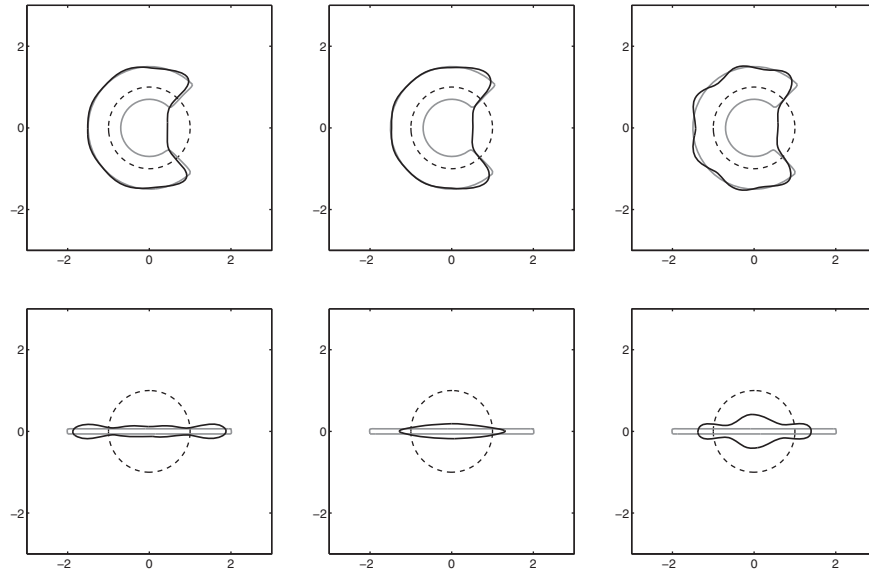


Figure 10. Reconstruction of C-shaped and bar-shaped inclusions by (from left to right) method 1, 2, and 3 after nine iterations.

generated at \mathbf{y}_m of direction γ_m^i can be expressed as follows:

$$\gamma_n^o \cdot (\mathbf{u}(\mathbf{y}_n, \mathbf{y}_m, \gamma_m^i) - \mathbf{G}^\omega(\mathbf{y}_n, \mathbf{y}_m) \gamma_m^i).$$

Note that pairs of transmitting and receiving elements could be repeated to model up to four experiments performed with the same pair of elements with orthogonal emission and reception directions γ_m^i and γ_n^o .

We assume that the characteristic size of the inclusion is much larger than $\pi c_p/\omega$. The problem we consider in this section is to image the extended elastic inclusion D from the MSR matrices at multiple frequencies $(\omega_p)_{p=1, \dots, P}$. There are many ways to exploit measurements at multiple frequencies; see, for example, [21]. Here we first sum the discrepancy functionals over frequencies. Second, we propose a hopping algorithm which uses recursively single-frequency measurements but at increasing frequencies.

9.2. Optimal control algorithms. In order to reconstruct the shape of an extended inclusion from the MSR matrices at multiple frequencies, we propose in this section a generalization of the algorithms designed in the first part of the paper to the elastic case. We propose optimal control algorithms to match the signal spaces of the MSR matrices at multiple frequencies. We want to find an inclusion D that minimizes the differences between the measured MSR matrices $\mathbf{A}_{\text{meas}}[\omega_p]$ and the computed matrix $\mathbf{A}[D, \omega_p]$, which is the MSR matrix associated with D at the frequency ω_p .

We first propose to minimize the cost functional:

$$(9.2) \quad \mathcal{J}_2[D] := \frac{1}{2P} \sum_p \sum_l W(\sigma_{\text{meas}}^{(l)}[\omega_p]) \left\| (\mathbf{A}[D, \omega_p] - \mathbf{A}_{\text{meas}}[\omega_p]) \mathbf{v}_{\text{meas}}^{(l)}[\omega_p] \right\|^2,$$

where $\sigma_{\text{meas}}^{(l)}[\omega_p]$ and $\mathbf{v}_{\text{meas}}^{(l)}[\omega_p]$ are respectively the significant singular values of $\mathbf{A}_{\text{meas}}[\omega_p]$ and the associated singular vectors. The minimization of the analogous of \mathcal{J}_1 is quite similar and will not be discussed here.

Analogously to \mathcal{J}_3 defined in (3.3), we introduce

$$(9.3) \quad \mathcal{J}_3[h_j] := \frac{1}{2P} \sum_p \sum_{l=1}^L \sum_{l'=1}^{L'} W(\sigma_{\text{meas}}^{(l)}[\omega_p]) W'(\sigma^{(l')}[\omega_p]) \left| \left\langle (\mathbf{A}[D^{h_j}, \omega_p] - \mathbf{A}_{\text{meas}}) \mathbf{v}_{\text{meas}}^{(l)}, \mathbf{v}^{(l')}[D_j, \omega_p] \right\rangle \right|^2,$$

where $\mathbf{v}^{(l')}[D_j]$, $j = 1, \dots, L'$, are the first L' singular vectors associated to $\sigma^{(l')}$.

Again the weights $W(\sigma_{\text{meas}}^{(l)})$ and $W'(\sigma^{(l)})$ are for enhancing all the detectable geometric features of the inclusion. As we have seen in the previous sections it can be appropriate to enhance the contributions of the singular vectors in the plunge region of the singular values in order to enhance the resolution of the edges of the inclusion.

We then compute the shape derivatives of $\mathcal{J}_2[D]$ and $\mathcal{J}_3[D]$. To do so, let $\boldsymbol{\nu}$ be the outward normal to ∂D , let $\boldsymbol{\tau}$ denote the tangential vector, and let κ be the curvature of ∂D . Let $h \in \mathcal{C}^1(\partial D)$ and consider $D^{\delta h}$ to be a δ -perturbation of D . The boundary $\partial D^{\delta h}$ is then given by

$$\partial D^{\delta h} = \{ \tilde{\mathbf{x}} : \tilde{\mathbf{x}} = \mathbf{x} + \delta h(\mathbf{x}) \boldsymbol{\nu}(\mathbf{x}), \mathbf{x} \in \partial D \}.$$

Consider the perturbed transmission problem

$$\begin{cases} \mathcal{L}_{\lambda, \mu} \mathbf{u}_\delta + \omega^2 \rho \mathbf{u}_\delta = -\gamma \delta \mathbf{y} & \text{in } \mathbb{R}^2 \setminus \overline{D^{\delta h}}, \\ \mathcal{L}_{\tilde{\lambda}, \tilde{\mu}} \mathbf{u}_\delta + \omega^2 \tilde{\rho} \mathbf{u}_\delta = \mathbf{0} & \text{in } D^{\delta h}, \\ \mathbf{u}_\delta|_+ - \mathbf{u}_\delta|_- = \mathbf{0} & \text{on } \partial D^{\delta h}, \\ \frac{\partial \mathbf{u}_\delta}{\partial n}|_+ - \frac{\partial \mathbf{u}_\delta}{\partial \tilde{n}}|_- = \mathbf{0} & \text{on } \partial D^{\delta h}, \\ \mathbf{u}_\delta \text{ satisfies the outgoing radiation conditions.} \end{cases}$$

We need to introduce some notation. Let $\mathbf{a} \otimes \mathbf{b} := (a_i b_j)_{i,j=1,2}$ denote the tensor product between vectors in \mathbb{R}^2 and let

$$(9.4) \quad \mathbf{E}[\mathbf{u}] = (E_{jl}[\mathbf{u}])_{j,l=1,2}, \quad E_{jl}[\mathbf{u}] = \frac{1}{2}(\partial_j u_l + \partial_l u_j).$$

Following exactly the same calculations as in [14] (see [5, 10]), we can prove that the leading-order term in the perturbations due to the interface changes is given by

$$(9.5) \quad \mathbf{u}_\delta(\mathbf{x}) - \mathbf{u}(\mathbf{x}) = \delta \left[\int_{\partial D} h(\mathbf{z}) \mathbf{M}[\mathbf{u}(\mathbf{z})] : \mathbf{E}[\mathbf{G}^\omega(\mathbf{z}, \mathbf{x})] d\sigma(\mathbf{z}) + \omega^2(\tilde{\rho} - \rho) \int_{\partial D} h(\mathbf{z}) \mathbf{G}^\omega(\mathbf{z}, \mathbf{x}) \mathbf{u}(\mathbf{z}) d\sigma(\mathbf{z}) \right] + o(\delta),$$

where the elastic moment tensor \mathbf{M} , which is now local, is given by

$$(9.6) \quad \mathbf{M}[\mathbf{u}] = a(\nabla \cdot \mathbf{u}) \mathbf{I} + b \mathbf{E}[\mathbf{u}] + c \left(\frac{\partial(\mathbf{u} \cdot \boldsymbol{\tau})}{\partial \tau} + \kappa \mathbf{u} \cdot \boldsymbol{\nu} \right) \boldsymbol{\tau} \otimes \boldsymbol{\tau} + d \frac{\partial(\mathbf{u} \cdot \boldsymbol{\nu})}{\partial \nu} \boldsymbol{\nu} \otimes \boldsymbol{\nu}$$

with

$$\begin{cases} a = (\tilde{\lambda} - \lambda) \frac{\lambda + 2\mu}{\tilde{\lambda} + 2\tilde{\mu}}, & b = 2(\tilde{\mu} - \mu) \frac{\mu}{\tilde{\mu}}, \\ c = 2(\tilde{\mu} - \mu) \left(\frac{2\tilde{\lambda} + 2\tilde{\mu} - \lambda}{\tilde{\lambda} + 2\tilde{\mu}} - \frac{\mu}{\tilde{\mu}} \right), & d = 2(\tilde{\mu} - \mu) \frac{\tilde{\mu}\lambda - \mu\tilde{\lambda}}{\tilde{\mu}(\tilde{\lambda} + 2\tilde{\mu})}. \end{cases}$$

Here $\mathbf{A} : \mathbf{B} = \sum a_{ij} b_{ij}$ for two matrices $\mathbf{A} = (a_{ij})$ and $\mathbf{B} = (b_{ij})$. The quantity $\mathbf{M}[\mathbf{u}(\mathbf{z})] : \mathbf{E}[\mathbf{G}^\omega(\mathbf{z}, \mathbf{x})]$ is a vector given by $(\mathbf{M}[\mathbf{u}(\mathbf{z})] : \mathbf{E}[\mathbf{G}^\omega(\mathbf{z}, \mathbf{x})])_l = \mathbf{M}[\mathbf{u}(\mathbf{z})] : \mathbf{E}[\mathbf{G}_l^\omega(\mathbf{z}, \mathbf{x})]$. A more compact but equivalent form of (9.6) can be found in [3].

Therefore, the shape derivative $d_S \mathcal{J}_2$ is given by

$$(9.7) \quad \begin{aligned} (d_S \mathcal{J}_2, h) &= \frac{1}{P} \operatorname{Re} \sum_p \sum_l W(\sigma_{\text{meas}}^{(l)}[\omega_p]) \\ &\quad \times \left\langle (\mathbf{A}[D, \omega_p] - \mathbf{A}_{\text{meas}}[\omega_p]) \mathbf{v}_{\text{meas}}^{(l)}[\omega_p], \right. \\ &\quad \left. \int_{\partial D} h(\mathbf{x}) \mathbf{B}[D, \omega_p](\mathbf{x}) \mathbf{v}_{\text{meas}}^{(l)}[\omega_p] d\sigma(\mathbf{x}) \right\rangle, \end{aligned}$$

where the matrix \mathbf{B} is defined by

$$\begin{aligned} B_{nm}[D, \omega_p](\mathbf{x}) &:= (\gamma_n^o)^T (\mathbf{M}[\mathbf{G}^{\omega_p}(\mathbf{x}, \mathbf{y}_m)] : \mathbf{E}[\mathbf{G}^{\omega_p}(\mathbf{x}, \mathbf{y}_n)]) \\ &\quad + \omega_p^2 (\tilde{\rho} - \rho) \mathbf{G}^{\omega_p}(\mathbf{x}, \mathbf{y}_m) \mathbf{G}^{\omega_p}(\mathbf{x}, \mathbf{y}_n) \gamma_m^i, \quad \mathbf{x} \in \partial D. \end{aligned}$$

The algorithm consists then in replacing, in each step, $\partial D \mapsto \partial D + h\nu$, where

$$(9.8) \quad \begin{aligned} h(\mathbf{x}) &= -\frac{1}{P} \operatorname{Re} \sum_p \sum_l W(\sigma_{\text{meas}}^{(l)}[\omega_p]) \\ &\quad \left\langle \mathbf{A}[D, \omega_p] - \mathbf{A}_{\text{meas}}[\omega_p], \mathbf{B}[D, \omega_p](\mathbf{x}) \mathbf{v}_{\text{meas}}^{(l)}[\omega_p] \right\rangle. \end{aligned}$$

Note that as in the scalar case, the action of $\mathbf{B}[D, \omega_p](\mathbf{x}) \mathbf{v}_{\text{meas}}^{(l)}[\omega_p]$ corresponds to back-propagating to ∂D the information in the MSR residual in the direction of the significant singular vectors of the measured MSR matrix. Using formula (9.5), one can easily compute the shape derivative of the cost functional \mathcal{J}_3 and design a second iterative procedure for reconstructing the elastic inclusion.

9.3. Finding an initial guess. We provide in this section an original algorithm for finding a good initial guess for the illuminated part of the boundary of the inclusion defined as the set of points $\mathbf{x} \in \partial D$ such that $(\mathbf{x} - \mathbf{y}_n) \cdot \nu(\mathbf{x}) < 0$ for some n :

$$\partial D_{\text{illum}} = \{\mathbf{x} \in \partial D : (\mathbf{x} - \mathbf{y}_n) \cdot \nu(\mathbf{x}) < 0\}.$$

The algorithm is based on a high-frequency analysis of the MSR matrices and is of migration type. In the high-frequency limit the P or compressional waves behave exactly like acoustic waves, while the S or shear waves behave exactly like electromagnetic waves [28]. The waves P and S are coupled by the transmission conditions.

In the elastic case, where the vector nature of the underlying elastic motion should be taken into consideration, the displacement field $\mathbf{u}(\mathbf{x})$, that is, the solution to (9.1), is the sum of a P and an S wave. Therefore, if one can migrate the parts of the MSR matrices corresponding to either the S or the P contribution, then one can form an initial guess for the illuminated part of the boundary of the inclusion.

Let us consider that for each point source \mathbf{y}_m , two experiments are carried out. In the l th experiment, $l = 1, 2$, a wave is emitted in the $\hat{\mathbf{e}}_l$ -direction and the reflected wave $\mathbf{u}_l(\mathbf{y}_n, \mathbf{y}_m)$ is recorded at each receiver point \mathbf{y}_n . Here $\hat{\mathbf{e}}_1 = (1, 0)^T$ and $\hat{\mathbf{e}}_2 = (0, 1)^T$. We can then form four response matrices:

$$(A_{nm}^{(jl)})_{n,m=1,\dots,N} = (\hat{\mathbf{e}}_j \cdot \mathbf{u}_l(\mathbf{y}_n, \mathbf{y}_m))_{n,m=1,\dots,N}, \quad j, l = 1, 2,$$

whose (n, m) th entry is the scalar field recorded at \mathbf{y}_n in the direction $\hat{\mathbf{e}}_j$ when a wave is emitted from \mathbf{y}_m in the direction $\hat{\mathbf{e}}_l$. These MSR matrices can be used to decompose the contributions of S and P parts, thanks to the following two remarks:

- By linearity, the vector velocity field recorded at \mathbf{y}_n when a wave is emitted from \mathbf{y}_m in the direction $\boldsymbol{\gamma}_m^i$ is $(\hat{\mathbf{e}}_1 \cdot \boldsymbol{\gamma}_m^i) \mathbf{u}_1(\mathbf{y}_n, \mathbf{y}_m) + (\hat{\mathbf{e}}_2 \cdot \boldsymbol{\gamma}_m^i) \mathbf{u}_2(\mathbf{y}_n, \mathbf{y}_m)$.
- The recorded vector displacement field can be decomposed into P and S wave modes. The P wave mode is characterized by a longitudinal velocity field (i.e., a velocity field oriented along the propagation axis), while the S wave mode is characterized by a transversal velocity field. As a result, for a given search point \mathbf{x} , denoting $\boldsymbol{\gamma}_n(\mathbf{x}) = (\mathbf{y}_n - \mathbf{x})/|\mathbf{y}_n - \mathbf{x}|$, the quantity

$$A_{nm}^{\mathbf{x}, PP} = \sum_{j,l=1}^2 (\hat{\mathbf{e}}_j \cdot \boldsymbol{\gamma}_n(\mathbf{x})) A_{nm}^{(jl)} (\hat{\mathbf{e}}_l \cdot \boldsymbol{\gamma}_m(\mathbf{x}))$$

gives the amplitude of the P wave coming from \mathbf{x} , recorded at \mathbf{y}_n , and emitted as a P wave from \mathbf{y}_m toward \mathbf{x} . We define similarly for the other mode components:

$$\begin{aligned} A_{nm}^{\mathbf{x}, PS} &= \sum_{j,l=1}^2 (\hat{\mathbf{e}}_j \cdot \boldsymbol{\gamma}_n(\mathbf{x})) A_{nm}^{(jl)} (\hat{\mathbf{e}}_l \cdot \boldsymbol{\gamma}_m(\mathbf{x})^\perp), \\ A_{nm}^{\mathbf{x}, SP} &= \sum_{j,l=1}^2 (\hat{\mathbf{e}}_j \cdot \boldsymbol{\gamma}_n(\mathbf{x})^\perp) A_{nm}^{(jl)} (\hat{\mathbf{e}}_l \cdot \boldsymbol{\gamma}_m(\mathbf{x})), \\ A_{nm}^{\mathbf{x}, SS} &= \sum_{j,l=1}^2 (\hat{\mathbf{e}}_j \cdot \boldsymbol{\gamma}_n(\mathbf{x})^\perp) A_{nm}^{(jl)} (\hat{\mathbf{e}}_l \cdot \boldsymbol{\gamma}_m(\mathbf{x})^\perp). \end{aligned}$$

As in the scalar case, we can then use the following Kirchhoff migration to get an initial guess:

$$\begin{aligned} \mathcal{I}_{\text{SM}}(\mathbf{x}) := \frac{1}{P} \sum_p \left[\overline{\mathbf{g}_P(\mathbf{x}, \omega_p)^T} A_{nm}^{\mathbf{x}, PP} \overline{\mathbf{g}_P(\mathbf{x}, \omega_p)} + \overline{\mathbf{g}_P(\mathbf{x}, \omega_p)^T} A_{nm}^{\mathbf{x}, PS} \overline{\mathbf{g}_S(\mathbf{x}, \omega_p)} \right. \\ \left. + \overline{\mathbf{g}_S(\mathbf{x}, \omega_p)^T} A_{nm}^{\mathbf{x}, SP} \overline{\mathbf{g}_P(\mathbf{x}, \omega_p)} + \overline{\mathbf{g}_S(\mathbf{x}, \omega_p)^T} A_{nm}^{\mathbf{x}, SS} \overline{\mathbf{g}_S(\mathbf{x}, \omega_p)} \right], \end{aligned}$$

where

$$\mathbf{g}_P(\mathbf{x}, \omega) = \left(\frac{\exp(i\frac{\omega}{c_p}|\mathbf{x} - \mathbf{y}_n|)}{\sqrt{N}} \right)_{n=1, \dots, N}, \quad \mathbf{g}_S(\mathbf{x}, \omega) = \left(\frac{\exp(i\frac{\omega}{c_s}|\mathbf{x} - \mathbf{y}_n|)}{\sqrt{N}} \right)_{n=1, \dots, N}.$$

10. Level-set and hopping algorithms. Level-set and hopping algorithms apply for both electromagnetic and elastic imaging of extended targets. The level-set algorithm is to handle topology changes such as breaking one component into two [29, 18], while the hopping algorithm is intended to improve the reconstruction results in a robust fashion by recursively using measurements at increasing frequencies [12].

10.1. Level-set reconstruction algorithm. The main idea of the level-set approach is to represent the inclusion D as the zero level set of a continuous function ϕ , i.e.,

$$D = \{ \mathbf{x} \in \Omega : \phi(\mathbf{x}) < 0 \},$$

to work with the function ϕ instead of an explicit representation, and to derive an evolution equation for ϕ to solve the maximization problem. In fact, by allowing additional time-dependence of ϕ , one can compute the geometric motion of D in time by evolving the level-set function ϕ . A geometric motion with normal velocity $V = V(\mathbf{x}, t)$ can be realized by solving the Hamilton–Jacobi equation

$$(10.1) \quad \frac{\partial \phi}{\partial t} + V(\mathbf{x}, t)|\nabla \phi| = 0.$$

Optimization within the level-set framework consists in choosing a velocity V driving the evolution toward a maximum (or at least increasing the objective functional we want to maximize).

In the elastic case, formula (9.8) gives the velocity V to choose within the level-set framework. One can convert the minimization problem (9.2) into a level-set form by choosing the gradient ascent direction $V(\mathbf{x})$ as

$$(10.2) \quad V(\mathbf{x}) = -\frac{1}{P} \operatorname{Re} \sum_p \sum_l W(\sigma_{\text{meas}}^{(l)}[\omega_p]) \left\langle (\mathbf{A}[D, \omega_p] - \mathbf{A}_{\text{meas}}[\omega_p]) \mathbf{v}_{\text{meas}}^{(l)}[\omega_p], \mathbf{B}[D, \omega_p](\mathbf{x}) \mathbf{v}_{\text{meas}}^{(l)}[\omega_p] \right\rangle.$$

Then we evolve ϕ by solving the Hamilton–Jacobi equation (10.1) for one time step. We emphasize that in (10.2), V is only defined on the boundary ∂D , even though under the level-set framework it has to be defined on the whole domain. We remark here that since $\boldsymbol{\nu} = \nabla \phi / |\nabla \phi|$, $\boldsymbol{\tau} = (\nabla \phi / |\nabla \phi|)^\perp$, $\boldsymbol{\kappa} = \nabla \cdot (\nabla \phi / |\nabla \phi|)$, it follows that

$$(10.3) \quad \mathbf{M}[\mathbf{u}] = c \left(\nabla \left(\mathbf{u} \cdot \left(\frac{\nabla \phi}{|\nabla \phi|} \right)^\perp \right) \cdot \left(\frac{\nabla \phi}{|\nabla \phi|} \right)^\perp + \left(\nabla \cdot \frac{\nabla \phi}{|\nabla \phi|} \right) \left(\mathbf{u} \cdot \frac{\nabla \phi}{|\nabla \phi|} \right) \right) \left(\frac{\nabla \phi}{|\nabla \phi|} \right)^\perp \\ \otimes \left(\frac{\nabla \phi}{|\nabla \phi|} \right)^\perp + a(\nabla \cdot \mathbf{u}) \mathbf{I} + b \mathbf{E}[\mathbf{u}] + d \frac{\nabla \phi}{|\nabla \phi|} \cdot \nabla \left(\mathbf{u} \cdot \frac{\nabla \phi}{|\nabla \phi|} \right) \frac{\nabla \phi}{|\nabla \phi|} \otimes \frac{\nabla \phi}{|\nabla \phi|}.$$

Therefore, (10.1) on ϕ can be modified as follows:

$$(10.4) \quad \frac{\partial \phi}{\partial t} + F \left(\frac{\nabla \phi}{|\nabla \phi|}, \nabla \cdot \frac{\nabla \phi}{|\nabla \phi|} \right) |\nabla \phi| = 0.$$

The evolution of the level-set function ϕ then follows from the solution of (10.4) instead of (10.1). Numerically, we start from an initial guess ϕ_0 for $\phi(\mathbf{x}, t)$ and evolve ϕ by (10.4) for one time step. We refer to [27] for more details on the level-set function and issues like reinitialization and regularization.

10.2. Hopping algorithm. Other than summing over the frequencies as in (4.6), a second approach for imaging extended inclusions from MSR matrices at multiple frequencies is by a hopping reconstruction method [12]. The data is assumed to be available at multiple frequencies, $\omega_1 < \dots < \omega_p$. The initial guess at step p is chosen from a level-set representation at frequency $\omega_{p-1}, p \geq 2$, obtained by minimizing the cost functional:

$$\mathcal{J}_2^{(p-1)}[D] := \sum_l W(\sigma_{\text{meas}}^{(l)}[\omega_{p-1}]) \left\| (\mathbf{A}[D, \omega_{p-1}] - \mathbf{A}_{\text{meas}}[\omega_{p-1}]) \mathbf{v}_{\text{meas}}^{(l)}[\omega_{p-1}] \right\|^2.$$

We can also use \mathcal{J}_3 . We can perform recursive linearization to improve the reconstruction for the inclusion. Let D_p be the reconstructed inclusion at step p using frequency $\omega_p, p \geq 1$. Suppose that ω_p is slightly larger than ω_{p-1} . We wish to determine the perturbation $D_p - D_{p-1}$. Writing, as in (9.8), $\partial D_p = \partial D_{p-1} + h\mathbf{v}$, we have

$$h(\mathbf{x}) = -\text{Re} \sum_l W(\sigma_{\text{meas}}^{(l)}[\omega_p]) \left\langle (\mathbf{A}[D_{p-1}, \omega_{p-1}] - \mathbf{A}_{\text{meas}}[\omega_p] + (\omega_p - \omega_{p-1}) \frac{d\mathbf{A}}{d\omega}[D_{p-1}, \omega_{p-1}]) \mathbf{v}_{\text{meas}}^{(l)}[\omega_p], \mathbf{B}[D_{p-1}, \omega_{p-1}](\mathbf{x}) \mathbf{v}_{\text{meas}}^{(l)}[\omega_p] \right\rangle.$$

Therefore, in order to determine D_p , one should only compute the additional quantity

$$\left(\frac{d\mathbf{A}}{d\omega}[D_{p-1}, \omega_{p-1}] \right) \mathbf{v}_{\text{meas}}^{(l)}[\omega_p].$$

11. Conclusion. In this paper we have proposed original optimization algorithms to recover geometric features of the shape of an inclusion using MSR matrices at single or multiple frequencies. In the first algorithm (the standard one), we minimize the discrepancy between the computed and measured MSR matrices. In the second one, the MSR discrepancy is minimized with respect to only the signal space, while in the third one, the MSR discrepancy of the search direction is minimized in the direction of the signal space. We have contrasted the second and third optimal control algorithms with the standard approach. The second and third algorithms yield shape reconstructions with better resolution. We have provided natural basis constructed by backpropagating the data for computing the shape changes. We have also formulated a new level-set-type approach and developed a weighted migration algorithm for finding a good initial guess. We have shown the optimality of the approach in the presence of a measurement noise. A hopping algorithm using an iterative level-set imaging procedure

was proposed. A detailed stability and resolution analysis for the proposed algorithms was performed in simplified configurations. We have considered both full- and limited-aperture imaging problems.

The presented numerical results (in the scalar case) show the efficiency of the proposed algorithms and their validity with respect to the size of the targets. The designed optimization algorithms perform numerically quite well and lead to stable and accurate reconstructions. It is found that the most standard method (method 1) is the most stable (if the size of the MSR matrix is small), while the third one based on backpropagating the singular vectors associated with the computed target has the best resolution. The degradation of the quality of the reconstructed image in the limited-view case and for imaging highly nonconvex targets is also illustrated. In the case where the MSR matrix is large, method 2 performs better than method 1 since the information in the noise space is filtered out. Note that the three algorithms have comparable complexities. Moreover, they use a gradient descent method to update the shape as shown in (4.5). Using higher order shape derivatives may not increase their resolution and stability properties.

In a forthcoming work, we will address the imaging of extended electromagnetic inclusions using the full Maxwell equations. We will also make an attempt to recover the material parameters of inhomogeneous extended targets from MSR measurements. To handle topology changes such as breaking one component into two, we will implement level-set versions of our algorithms.

Appendix A. Prolate spheroidal functions. We review some results that are taken from [25, 30] and that are relevant for our paper. Let $C > 0$. The prolate spheroidal functions $\psi^{(l)}(x)$ are the eigenfunctions of the sinc kernel:

$$(A.1) \quad \int_{-1}^1 \frac{\sin[C(x-y)]}{\pi(x-y)} \psi^{(l)}(y) dy = \sigma^{(l)} \psi^{(l)}(x).$$

The symmetric sinc kernel $\frac{\sin C(x-y)}{\pi(x-y)}$ is positive definite. Its spectrum $(\sigma^{(l)})_{l \geq 1}$ is discrete and positive, $\sigma^{(1)} > \sigma^{(2)} > \dots > 0$ and $\sigma^{(l)} \rightarrow 0$ as $l \rightarrow \infty$. The real-valued eigenfunctions $\psi^{(l)}$ are orthonormal on $(-1, 1)$ (they can be continued to define orthogonal functions on $(-\infty, \infty)$):

$$(A.2) \quad \int_{-1}^1 \psi^{(l)}(x) \psi^{(j)}(x) dx = \delta_{jl},$$

where δ_{jl} denotes the Kronecker symbol.

By the spectral representation of the sinc kernel, we have

$$(A.3) \quad \sum_{l=1}^{\infty} \sigma^{(l)} \psi^{(l)}(x) \psi^{(l)}(y) = \frac{\sin[C(x-y)]}{\pi(x-y)} \quad \text{for } x, y \in (-1, 1),$$

$$(A.4) \quad \sum_{l=1}^{\infty} \psi^{(l)}(x) \psi^{(l)}(y) = \delta(x-y) \quad \text{for } x, y \in (-1, 1).$$

When C is large, the eigenvalues $\sigma^{(l)}$ stay close to one for small l and then they plunge to 0

near the threshold value $[2C/\pi]$:

$$(A.5) \quad \sigma^{(l)} \xrightarrow{C \rightarrow \infty} \begin{cases} 1 & \text{if } l = \left[\frac{2C}{\pi}(1 - \varepsilon) \right], \quad \varepsilon > 0, \\ \frac{1}{1 + e^{\pi b}} & \text{if } l = \left[\frac{2C}{\pi} + \frac{b}{\pi} \log C \right], \quad b \in \mathbb{R}, \\ 0 & \text{if } l = \left[\frac{2C}{\pi}(1 + \varepsilon) \right], \quad \varepsilon > 0. \end{cases}$$

Finally, we have for any $x \in \mathbb{R}$ and $l \geq 1$

$$(A.6) \quad \int_{-1}^1 e^{-iCxy} \psi^{(l)}(y) dy = i^{l+1} \sqrt{\frac{2\pi\sigma^{(l)}}{C}} \psi^{(l)}(x).$$

Acknowledgments. The authors are very grateful to the reviewers for their comments and suggestions to improve the presentation of the paper.

REFERENCES

- [1] M. ABRAMOWITZ AND I. STEGUN, EDS., *Handbook of Mathematical Functions*, National Bureau of Standards, Washington, DC, 1964.
- [2] H. AMMARI, E. BERETTA, E. FRANCINI, H. KANG, AND M. LIM, *Optimization algorithm for reconstructing interface changes of a conductivity inclusion from modal measurements*, *Math. Comp.*, 79 (2010), pp. 1757–1777.
- [3] H. AMMARI, E. BERETTA, E. FRANCINI, H. KANG, AND M. LIM, *Reconstruction of small interface changes of an inclusion from modal measurements II: The elastic case*, *J. Math. Pures Appl.*, 94 (2010), pp. 322–339.
- [4] H. AMMARI, P. CALMON, AND E. IAKOVLEVA, *Direct elastic imaging of a small inclusion*, *SIAM J. Imaging Sci.*, 1 (2008), pp. 169–187.
- [5] H. AMMARI, P. GARAPON, F. JOUVE, H. KANG, M. LIM, AND S. YU, *A new optimal control approach for the reconstruction of extended inclusions*, *SIAM J. Control and Optim.*, in revision.
- [6] H. AMMARI, J. GARNIER, H. KANG, W.K. PARK, AND K. SØLNA, *Imaging schemes for perfectly conducting cracks*, *SIAM J. Appl. Math.*, 71 (2011), pp. 68–91.
- [7] H. AMMARI, J. GARNIER, AND K. SØLNA, *A statistical approach to target detection and localization in the presence of noise*, *Waves Random Complex Media*, to appear.
- [8] H. AMMARI AND H. KANG, *Reconstruction of Small Inhomogeneities from Boundary Measurements*, *Lecture Notes in Math.* 1846, Springer-Verlag, Berlin, 2004.
- [9] H. AMMARI, H. KANG, E. KIM, AND J.Y. LEE, *The generalized polarization tensors for resolved imaging. Part II: Shape and electromagnetic parameters reconstruction of an electromagnetic inclusion from multistatic measurements*, *Math. Comp.*, 81 (2012), pp. 839–860.
- [10] H. AMMARI, H. KANG, AND H. LEE, *Layer Potential Techniques in Spectral Analysis*, *Math. Surveys Monogr.* 153, American Mathematical Society, Providence, RI, 2009.
- [11] H. AMMARI, H. KANG, G. NAKAMURA, AND K. TANUMA, *Complete asymptotic expansions of solutions of the system of elastostatics in the presence of inhomogeneities of small diameter*, *J. Elasticity*, 67 (2002), pp. 97–129.
- [12] G. BAO, S. HOU, AND P. LI, *Recent Studies on Inverse Medium Scattering Problems*, *Lecture Notes in Comput. Sci. Engrg.* 59, Springer-Verlag, Berlin, 2007, pp. 165–186.
- [13] E. BERETTA AND E. FRANCINI, *Asymptotic formulas for perturbations in the electromagnetic fields due to the presence of thin inhomogeneities*, in *Inverse Problems: Theory and Applications*, *Contemp. Math.* 333, American Mathematical Society, Providence, RI, 2003.
- [14] E. BERETTA AND E. FRANCINI, *An asymptotic formula for the displacement field in the presence of thin elastic inhomogeneities*, *SIAM J. Math. Anal.*, 38 (2006), pp. 1249–1261.
- [15] M. BONNET AND B.B. GUZINA, *Elastic-wave identification of penetrable obstacles using shape-material sensitivity framework*, *J. Comput. Phys.*, 228 (2009), pp. 294–311.

- [16] L. BORCEA, G. PAPANICOLAOU, AND C. TSOGKA, *Optimal waveform design for array imaging*, Inverse Problems, 23 (2007), pp. 1973–2021.
- [17] L. BORCEA, G. PAPANICOLAOU, AND F.G. VASQUEZ, *Edge illumination and imaging of extended reflectors*, SIAM J. Imaging Sci., 1 (2008), pp. 75–114.
- [18] O. DORN AND D. LESSELIER, *Level-sets for solutions of inverse scattering problems*, Inverse Problems, 22 (2006), 085001.
- [19] A. ERDÉLYI, W. MAGNUS, F. OBERHETTINGER, AND F.G. TRICOMI, EDs., *Higher Transcendental Functions*, vol. II, McGraw-Hill, New York, 1953.
- [20] J. GARNIER AND G. PAPANICOLAOU, *Resolution analysis for imaging with noise*, Inverse Problems, 26 (2010), 074001.
- [21] B.B. GUZINA, F. CAKONI, AND C. BELLIS, *On the multi-frequency obstacle reconstruction via the linear sampling method*, Inverse Problems, 26 (2010), 125005.
- [22] S. HOU, K. SØLNA, AND H. ZHAO, *A direct imaging algorithm for extended targets*, Inverse Problems, 22 (2006), pp. 1151–1178.
- [23] S. HOU, K. SØLNA, AND H. ZHAO, *Imaging of location and geometry for extended targets using the response matrix*, J. Comput. Phys., 199 (2004), pp. 317–338.
- [24] J.B. KELLER AND R.M. LEWIS, *Asymptotic methods for partial differential equations: The reduced wave equation and Maxwell's equations*, in Surveys in Applied Mathematics, vol. 1, J.B. Keller, D.W. McLaughlin, and G.C. Papanicolaou, eds., Plenum Press, New York, 1995, pp. 1–82.
- [25] H.J. LANDAU AND H. WIDOM, *The eigenvalue distribution of time and frequency limiting*, J. Math. Anal. Appl., 77 (1980), pp. 469–481.
- [26] J. NOCEDAL AND S.J. WRIGHT, *Numerical Optimization*, Springer-Verlag, New York, 1999.
- [27] S. OSHER AND J.A. SETHIAN, *Fronts propagating with curvature-dependent speed: Algorithms based on Hamilton-Jacobi formulations*, J. Comput. Phys., 79 (1988), pp. 12–49.
- [28] L. RYZHIK, G. PAPANICOLAOU, AND J.B. KELLER, *Transport equations for elastic and other waves in random media*, Wave Motion, 24 (1996), pp. 327–370.
- [29] F. SANTOSA, *A level-set approach for inverse problems involving obstacles*, Control Optim. Calcul. Var., 1 (1996), pp. 17–33.
- [30] D. SLEPIAN, *Some comments on Fourier analysis, uncertainty and modeling*, SIAM Rev., 25 (1983), pp. 379–393.
- [31] R. WONG, *Asymptotic expansion of $\int_0^{\pi/2} J_\nu^2(\lambda \cos \theta) d\theta$* , Math. Comput., 50 (1988), pp. 229–234.
- [32] H. ZHAO, *Analysis of the response matrix for an extended target*, SIAM J. Appl. Math., 64 (2004), pp. 725–745.